# USING COMPUTER SIMULATIONS TO STUDY RELATIVISTIC HEAVY ION COLLISIONS

By

Joelle Murray

A DISSERTATION

Submitted to
Michigan State University
in partial fulfillment of the requirements
for the degree of

DOCTOR OF PHILOSOPHY

Department of Physics and Astronomy

1998

# ABSTRACT

## USING COMPUTER SIMULATIONS TO STUDY RELATIVISTIC HEAVY ION COLLISIONS

By

Joelle Murray

One of the most exciting topics in high-energy nuclear physics is the study of the potential phase transition between hadronic and partonic matter. Information about this transition, if it exists and can be experimentally determined, would be vital in understanding confinement of quarks and gluons inside hadrons. New accelerators, RHIC and LHC, will be online in the next few years and will focus on finding evidence for this transition. RHIC will collide Au on Au at center of mass energies equal to 200 $GeV$/nucleon and create a high density, high temperature state of matter. To study the large particle multiplicities that will occur at these experiments, computer simulations are being developed. Within this thesis, one type of simulation will be detailed and used to study the invariant mass spectrum of leptons pairs measured at CERN SPS and several hadronic observables that could be measured at RHIC.

There are far too many people to thank– my family: Aidan. Joel. Shannon. Todd. Mom. and Dad-for their unconditional support and advice: Dr. Wolfgang Bauer-for his infinite patience. wit. and wisdom: Dr. Gerald Pollack. Dr. Wayne Repko. Dr. Scott Pratt. and Dr. Kevin Haglin-for invaluable guidance: fellow graduate students and friends: Jon Kruse. Sal Fahey. Don Anthony. Gerd Kortemeyer. Njema Frazier. Dave Brown. Frank Daffin. Alexander Volya. Mike Wiest. Kate Frame. Gian DiLoreto. Steve Grice. Jennifer Huggler. Lisa Schell. Ken Marshall. Lisa Wolford. and Quentin Brasky-for keeping me sane.

# Contents

# List of Figures

# Chapter 1

# Introduction

One of the great challenges facing experimental high-energy and nuclear physics during the next decade is determining the nature of the transition from hadronic to quark-gluon degrees of freedom. This transition must exist at sufficient temperature since hadronic degrees of freedom are inappropriate once densities exceed the normal inverse volume of a hadron, approximately 1 $fm^{-3}$. These conditions should be realized inside the reaction zone of an ultra-relativistic collision of two heavy ions. For this reason the Relativistic Heavy Ion Collider (RHIC), which will collide gold nuclei with energies of 200 $GeV$/nucleon, is under construction at Brookhaven; and the LHC at CERN, which will collide heavy ions with energies of 6300 $GeV$/nucleon, has recently been approved.

Lattice gauge calculations have shown evidence that a first order phase transition between confined hadronic matter and deconfined QCD matter may exist for nuclear collisions at very high energy density. [1]. By studying this phase transition, a better understanding of how and why quarks and gluons are confined within hadronic matter can be obtained. Perhaps the most important issue regarding the deconfinement transition is whether it is first order with a large latent heat. If this is true the pressure would be greatly reduced compared to a free gas, resulting in noticeably less collective flow in collisions. However, in order to determine the equation of state from the flow inferred from measurements after the reaction, it is necessary to understand the initial conditions of the collision. In a high-energy collision, partons, not hadrons, represent the appropriate degrees of freedom. With this motivation, parton cascade models [2, 3] have been developed to simulate the initial prethermalized stage of the reaction. A parton cascade incorporates the established theory of perturbative QCD within the space-time evolution of a heavy ion collision. Extracting information from the parton cascade will hopefully lead to predictions of signals for the quark-gluon plasma that can be detected at RHIC and the LHC at CERN.

Although the potential information parton cascades could yield is substantial, they are severely limited by available knowledge and whether or not a quark-gluon plasma is even formed during the collision. Experimental detection of the quark-gluon plasma depends largely on the characteristics of the collision in its absence, something we shall call background. In order to better quantify this background, simulations without "built-in" plasma formation that still assume a QCD description of nucleon scattering must be explored. HIJING, developed by Wang and Gyulassy[4], is precisely this type of model and has been used to look at multiple minijet production, shadowing and jet quenching in pA and AA collisions.

By comparing these two types of models to one another, signals denoting plasma formation can more easily be determined. Comparisons of these simulations to experiment can provide information on the basic properties of interactions between the fundamental components of matter.

Within this thesis, a review of the parton model, perturbative QCD, and parton cascades will be given first. Then a non-cascade, background, simulation will be detailed as well as two avenues of study using this simulation. At this energy and density, many different factors contribute to the overall spectra that do not contribute in lower energy collisions. Both studies will focus in on the role of secondary scattering in final state observables. The first study presented is of dilepton production relevant to the CERN SPS experiment that investigated the invariant mass distribution of low-mass lepton pairs and their sources. The second study looks at hadronic spectra from collisions of Au+Au at $\sqrt{s} = 200\ GeV$/nucleon. Finally, conclusions and a discussion of future investigations that can be performed with this simulation are made.

# Chapter 2

# Parton Model, Perturbative QCD and PYTHIA/JETSET overview

Before describing a model for high energy heavy ion collisions, it is necessary to understand the physics governing the underlying nucleon-nucleon collisions. At RHIC and LHC, the center of mass energies per nucleon is on the order of several hundred to several thousand $GeV$. This means that the heavy ion collisions performed at these accelerators will be able to probe distances much smaller than the typical size of a hadron. For this reason, one must use parton degrees of freedom instead of hadronic ones to describe the nucleon scattering at RHIC and LHC energies. The basics of high energy nucleon-nucleon scattering will be reviewed in the next few sections via descriptions of the parton model [6], deep inelastic scattering [7], perturbative Quantum Chromodynamics (pQCD), the QCD-improved parton model and the workings of a high-energy event generator, PYTHIA/JETSET [5].

## 2.1 Parton Model and Deeply Inelastic Scattering (DIS)

The first model attempting to describe the structure of hadrons was the quark model [8]. It was independently developed by Gell-Mann and Zweig and asserts that hadrons have structure and consist of elementary particles called quarks. Quarks occur in three types: u, d, s and have fractional charge. The proposed quarks neatly explained the structure of the Eight-Fold Way [9], a classification scheme for hadrons also developed by Gell-Mann.

Proof of this theory was difficult as experiments are not able to isolate single quarks. In the late 1960's, an experiment was performed at SLAC that looked at the hard scattering of leptons with hadron. This type of experiment is known as Deeply Inelastic Scattering (DIS) [7], Figure 2.1. DIS provided an opportunity to exploit the well-established theory of QED to discover information about the structure of hadrons. Within QED, the matrix element squared for a DIS event, $ep \rightarrow eX$, can be taken to be

$$< |\mathcal{M}|^2 >= \frac{g_e^4}{q^4} \mathcal{L}^{\mu\nu} K_{\mu\nu}(X) \tag{2.1}$$

where the leptonic tensor, $L_{\mu\nu}$, contains information on the electron state and the coupling between the electron and photon. The hadronic tensor, $K_{\mu\nu}$, is dependent on quantities such as the proton's momentum and should describe $\gamma^* p \rightarrow X$. Based on this combination of knowns and unknowns, the cross section can be written as

$$\frac{d^2\sigma}{dE'd\Omega} = (\frac{\alpha}{4E'\sin^2\theta/2})^2[2W_1\sin^2\theta/2 + W_2\cos^2\theta/2] \tag{2.2}$$

where $W_1$ and $W_2$ are form factors for the structure of the proton and $E$ ($E'$) are the initial (final) energies of the electron. This formulation works well for low-energy scattering where elastic scattering dominates, but fails at higher energies where the proton is broken up by the collision.

The offshell mass of the photon, $Q^2$, is related to its wavelength by $\lambda \sim \sqrt{1/(-Q^2)}$ and the wavelength of the virtual photon in DIS is the quantity that determines the amount of proton structure the photon is capable of seeing. If the virtual photon's offshell mass is small, it is unable to probe the structure inside the proton and is only able to give information on the size of the proton, it's charge and magnetic moment. By increasing the offshell mass of the photon so that its corresponding wavelength is smaller than the size of the proton ($\lambda \sim 1$ $fm$), the structure of the proton may be resolved.

As a consequence of this picture, Bjorken proposed that the form factors for DIS should scale as a function of this offshell mass as scattering energies increase [10]. This means that $W_1$ and $W_2$ in Equation 2.2 should not be functions of $Q^2$ at high energies. Bjorken scaling was verified at the DIS experiments at SLAC. The presence of this scaling, allows for the interpretation that the virtual photon is actually scattering off of a point-like particle inside the proton. Assuming that the proton is composed of point-like particles, the structure functions $W_1$ and $W_2$ become simple delta functions.

$$2W_1{}^{point} = \frac{Q^2}{2m^2}\delta(E - E' - Q^2/2m) \tag{2.3}$$

$$W_2{}^{point} = \delta(E - E' - Q^2/2m) \tag{2.4}$$

The discovery of Bjorken scaling, led to the development of the parton model [6]. The parton model asserts that the proton consists of point-like particles, partons, and that they each carry different momentum fractions, $x$, of the proton's momentum. Calculations involving this assertion are only valid in a frame where the proton's momentum is much larger than its mass (the infinite momentum frame). This is consistent with the fact that partons can only be "seen" when the collisions are very energetic. The parton distribution, $f(x)$, serves as the link between parton- and hadron-level information. By definition, it describes the probability density that the parton considered has momentum $xp$, where $p$ is the momentum of the proton. With this definition, the probability, $xf(x)$, when summed over all parton types and integrated over all possible momentum fractions, $x$, should be one. This conservation of probability (momentum) is represented by the following sum over all parton types.

$$\sum \int x f(x) dx = 1 \tag{2.5}$$

The relationship between parton distributions and the experimentally measurable structure functions. $W_2$ and $W_2$. allows for phenomenological determination of parton distributions. The following equations quantifies this relationship.

$$W_1 = \frac{1}{2M} \sum_i q_i^2 f_i(x) \tag{2.6}$$

$$W_2 = -\frac{2M}{Q^2} x^2 \sum_i q_i^2 f_i(x) \tag{2.7}$$

where $q_i$ is the fractional charge of each parton type.

Once there was experimental confirmation of the presence of particles inside protons. the previously proposed quark model could be connected to the parton model and Bjorken's partons also became synonymous with Gell-Mann's quarks.

At the simplest level. QCD sum rules provide a constraint for the types of quarks inside a hadron by requiring that the charge of all the quarks inside of a hadron sum up to the charge of the hadron. The following rules are for the quark structure of the proton.

$$\int (u(x) - \bar{u}(x)) dx = 2 \tag{2.8}$$

$$\int (d(x) - \bar{d}(x)) dx = 1 \tag{2.9}$$

$$\int (s(x) - \bar{s}(x)) dx = 0 \tag{2.10}$$

The first and second equations state that the number of anti-u(d) quarks subtracted from the number of u(d) quarks should be 2(1). This is because the fractional charge of u quarks is 2/3 and the fractional charge of d quarks is -1/3. Since all of the charge in a proton is accounted for by the u and d quarks. the total charge of strange and anti-strange quarks should add up to zero. This last constraint is also consistent with the fact that the proton's "strangeness" is zero.

The parton model was able to explain scaling in DIS and identify quarks as partons. but it still needed justification in quantum field theory [13].

## 2.2 Perturbative QCD overview

The field theory of particles that interact through the electromagnetic coupling. Quantum Electrodynamics (QED). was developed by Tomononaga. Feynman. and Schwinger in the 1940's. This theory established quantitative field theoretical methods for describing interactions between charged particles and photons.

Noether's Theorem states that for every symmetry that occurs in nature there is a conserved quantity associated with it and vice versa. It was noticed that interactions between charged particles always conserve charge. This conservation can be associated with the symmetry group of rotations U(1). It was on this basis that the field theory. Quantum Electrodymanics. was founded.

Drawing on the lessons learned in the development of QED. Quantum Chromodynamics was developed. Instead of electrons and photons. QCD looks at the strong interactions between the constituents of nucleons. quarks and gluons.

The conserved quantity important in QED is charge whereas in QCD it is a quantity called color charge. Although charge is an experimentally measurable quantity. color charge is not. Only colorless or color-singlet objects are observed. The symmetry group associated with this quantity is SU(3).

The QCD Lagrangian. describing a non-abelian SU(3) gauge theory. results in a more complex coupling between quarks and gluons than QED has for leptons and photons.

$$\mathcal{L} = \bar{q}(i\gamma^{\mu}\partial_{\mu} - m)q - g_s(\bar{q}\gamma^{\mu}\mathbf{T}_a q)G_{\mu}{}^{a} - \frac{1}{4}G_{\mu\nu}{}^{a}G_{a}{}^{\mu\nu} \tag{2.11}$$

where q is a Dirac spinor representing a quark state and $G_{\mu}{}^{a}$ refers to the gluon field. $\mathbf{T_a}$ are the generators of the SU(3) group governed by the following commutation relation: $[\mathbf{T_a}, \mathbf{T_b}] = i f_{abc}\mathbf{T_c}$. The gluon field strength tensor is represented by $G_{\mu\nu}{}^{a}$.

$$G_{\mu\nu}{}^{a} = \partial_{\mu}G_{\nu}{}^{a} - \partial_{\nu}G_{\mu}{}^{a} - i f_{abc}G_{\mu}{}^{b}G_{\nu}{}^{c} \tag{2.12}$$

The Lagrangian in Equation 2.11 (shown without gauge fixing and ghost terms) is used to derive a set of rules for calculating pQCD quantities. With these rules, Feynman diagrams can be constructed that represent the appropriate coupling between the particles considered. These diagrams must represent all possible combinations of couplings to remain invariant under any gauge transformation. The QCD tree-level $2 \rightarrow 2$ processes important for nucleon-nucleon scattering are

$$qq \rightarrow qq,\ qq' \rightarrow qq',\ qg \rightarrow qg$$
$$q\bar{q} \rightarrow q'\bar{q}',\ q\bar{q} \rightarrow q\bar{q},\ gg \rightarrow gg$$

Gluons account for a large fraction of the nucleon's momenta. Therefore, the processes containing gluons in the initial state account for most of the cross section in pQCD. From the Lagrangian, a gauge invariant set of Feynman diagrams can be determined. Diagrams for the process $qg \rightarrow qg$ are shown in Figure 2.2. The matrix elements that result from those diagrams are shown in the following equations.

$$\mathcal{M}_s = -\frac{g_s{}^2}{s}\bar{u}_2[\mathbf{T_b}\mathbf{T_a}\gamma_{\mu}(\not{p}_1 + \not{k}_1)\gamma_{\nu}]u_1\epsilon_1{}^{\nu}\epsilon_2{}^{\mu} \tag{2.13}$$

$$\mathcal{M}_t = i\frac{g_s{}^2}{t}f^{abc}\mathbf{T_c}\bar{u}_2F_{\mu\nu\lambda}\gamma_{\lambda}u_1\epsilon_1{}^{\mu}\epsilon_2{}^{\nu} \tag{2.14}$$

$$F_{\mu\nu\lambda} = g_{\mu\nu}(k_1 + k_2)_{\lambda} + g_{\nu\lambda}(k_1 - 2k_2)_{\mu} + g_{\lambda\mu}(k_2 - 2k_1)_{\nu} \tag{2.15}$$

$$\mathcal{M}_u = -\frac{g_s{}^2}{u}\bar{u}_2[\mathbf{T_a}\mathbf{T_b}\gamma_{\mu}(\not{p}_1 - \not{k}_2)\gamma_{\nu}]u_1\epsilon_2{}^{\nu}\epsilon_1{}^{\mu} \tag{2.16}$$

where $p_1$, $p_2$, $u_1$, and $\bar{u}_2$ are the momenta and Dirac spinors representing the incoming and outgoing quarks. The incoming and outgoing gluons momenta and polarization are represented by $k_1$, $k_2$, $\epsilon_1$, and $\epsilon_2$. The Mandelstam variables $\hat{s}$, $\hat{t}$, and $\hat{u}$ are defined by the following equations: $\hat{s} = (p_1 + k_1)^2$, $\hat{t} = (p_1 - p_2)^2$, and $\hat{u} = (p_1 - k_2)^2$. The $\hat{t}$-channel diagram includes a three gluon coupling which is not possible among the vector bosons in QED.

The sum of the matrix elements squared, summed over color and averaged over spin and color, is related to the cross section for each process by

$$\frac{d\hat{\sigma}}{d\hat{t}} = \frac{< |\mathcal{M}|^2 >}{16\pi \hat{s}^2} \tag{2.17}$$

in the center of momentum frame. For $qg$ scattering, the differential cross section is

$$\frac{d\hat{\sigma}}{d\hat{t}} = \frac{\pi {\alpha_s}^2}{\hat{s}^2}\left(\frac{\hat{s}^2 + \hat{u}^2}{\hat{t}^2} - \frac{4}{9}\frac{\hat{s}^2 + \hat{u}^2}{\hat{s}\hat{u}}\right) \tag{2.18}$$

The theory described by the QCD Lagrangian must be renormalizable, where renormalization is the process of absorbing very-short distance scale physics into a few parameters [11]. Therefore, the coupling strength $g_s$ depends on the renormalization scale $\mu$ and, to leading order, takes on the following form:

$$\alpha_s \equiv \frac{{g_s}^2}{4\pi} = \frac{4\pi}{b_1 ln(\mu^2/{\Lambda_{QCD}}^2)} \tag{2.19}$$

where $b_1 = (11\ N_c - 2\ n_f)/3$ with $N_c$ as the number of colors and $n_f$ as the number of flavors within the theory. The renormalized coupling decreases at large momentum scales and allows for a valid perturbative expansion of Feynman diagrams: similar to the formalism used in QED. This consequence is known as asymptotic freedom [12] and implies that at large momentum scales (short distance scales), partons inside hadrons rarely interact with one another.

## 2.3 The QCD-Improved Parton Model

Several of the integral properties of pQCD lead to important improvements in the calculational power of the parton model. These inclusions define the QCD-improved parton model [11. 13. 14]. Asymptotic freedom allows for factorization of the short distance (perturbative) behaviour from the long distance (non-perturbative) behaviour. For DIS. Figure 2.1. the physical cross section for $e^-p \rightarrow e^-X$ can be factorized into two parts.

$$\sigma_{e^-p\rightarrow e^-X}(s.Q) = \sum_a f_p{}^a(x.\mu) \otimes \hat{\sigma}_{e^-q_a\rightarrow e^-q_a}(\hat{s}.Q.\mu) \tag{2.20}$$

where $\sqrt{s}$ is the c.m. energy of the virtual photon/proton system. $\sqrt{\hat{s}}$ is the c.m. energy of the virtual photon/parton system. $Q$ is the probing energy scale. and $\mu$ is the renormalization scale. The renormalization scale separates the non-perturbative parton distribution function. $f_p{}^a(x.\mu)$. from the perturbative. parton-level inclusive cross section. $\hat{\sigma}_{e^-q_a\rightarrow e^-q_a}$.

One further consequence of factorization is that the physical cross section cannot depend on the renormalization scale $\mu$. This condition leads to evolution equations for parton distribution functions. known as DGLAP equations [15]. To first order. the evolution equations for quark and gluon distributions are as follows.

$$\frac{d}{dln\mu_F^2}q_{u/h}(x.\mu_F^2) = \frac{\alpha_s(\mu_F^2)}{2\pi}\int_x^1 \frac{dy}{y}[q_{a/h}(y.\mu_F^2)P_{qq}(\frac{x}{y}) + g(y.\mu_F^2)P_{qg}(\frac{x}{y})] \tag{2.21}$$

$$\frac{d}{dln\mu_F^2}g(x.\mu_F^2) = \frac{\alpha_s(\mu_F^2)}{2\pi}\int_x^1 \frac{dy}{y}[\sum_b q_{b/h}(y.\mu_F^2)P_{gq}(\frac{x}{y}) + g(y.\mu_F^2)P_{gg}(\frac{x}{y})] \tag{2.22}$$

The splitting functions. $P_{qq}$. $P_{qg}$. $P_{gg}$ [15]. are calculable within pQCD. These functions describe the probability that a parton with momentum fraction $y$ can be found inside a parton with momentum fraction $x$. These equations can be used to aid in determining the parton distribution functions at different energy scales.

Determining the gluon distribution poses a special challenge, as it is not constrained by QCD sum rules similar to those in Equation 2.8-2.10 and does not couple directly to non-QCD particles. Various experiments are used to constrain parton distributions; such as DIS, Drell-Yan, and direct photon studies. More current methods for pinning down the gluon structure function involve global analysis of all available data. This has been investigated extensively by the CTEQ collaboration [16, 17, 18] and structure functions have been determined more accurately [17] in the region of low-momentum fractions, Figure 2.3.

The evolution equation-improved parton distributions coupled with pQCD through factorization allows theoretical predictions of certain physical cross sections to be made. These advances in calculational techniques served as inspiration for high-energy event generators; one of which, PYTHIA/JETSET, will be described in the next section.

## 2.4 PYTHIA/JETSET overview

Now that a basis has been set for using pQCD and the QCD-improved parton model, one needs a better understanding of the event generator the heavy-ion model, described in the fourth chapter, is based on. PYTHIA with JETSET [5] is a Monte-Carlo type simulation that models high-energy collisions between hadrons and leptons with an emphasis on multiple particle production through collisions between elementary particles. The simulation is based on the premise of the QCD-improved parton model and employs cross sections calculated within perturbative QCD. PYTHIA/JETSET is able to simulate the scattering of a variety of hadrons (including mesons) and leptons from the initial to final state with a similar amount of detail as experimentally observable events.

For the purposes of the physics described in this section, only nucleon-nucleon scattering is of interest. In the following sections, a general description of the program will be given as well as a sample program and output. A general outline of the PYTHIA/JETSET program can be broken up into the following categories [5]:

1. The two beam particles move toward one another and their partonic structure is characterized by parton distribution functions.
2. One parton from each beam particle can sequentially branch (for example $q \rightarrow qg$) and build up a shower of initial state partons.
3. One parton from each initial shower participates in the hard process, where two outgoing partons are produced.
4. The outgoing partons can also branch and create final state showers.
5. When the initiator partons are removed from the beam particles, a beam remnant is left behind with a partonic structure and net color charge related to the final state partons.
6. Confinement requires that color charged individual quarks are not observed in the final state. Colorless strings are formed from the final state partons, radiated partons, and beam remnants.
7. The strings are fragmented into hadrons and the unstable produced hadrons decay further.

These categories will be described in more detail in the following sections.

### 2.4.1 Initialization and Scattering

During this stage of the program, the configuration (beam particle types, momenta, and frame of collision) of the initial system is used to determine the type of scattering that will take place between beam particles. There are several types of scattering PYTHIA can model: elastic, diffractive, or inelastic. The elastic and diffractive cross sections are parameterized to match existing data. PYTHIA is equipped with two different types of inelastic scattering; low-pt and hard scattering. Low-pt scattering cross sections are determined by parameterizations based on non-perturbative physics

$$\sigma_{tot}{}^{AB}(s) = X^{AB}s^{\epsilon} + Y^{AB}s^{-\eta} \qquad (2.23)$$

where $\sqrt{s}$ is the center of mass energy. The parameters $\epsilon$ and $\eta$ are universal, phenomenologically determined constants whereas $X^{AB}$ and $Y^{AB}$ are specific to each initial state [19]. High-pt or hard scattering cross sections are determined by perturbative QCD.

The remaining description will relate to the simulation of hard collisions between nucleons. For hard (high-pt) inelastic scattering, a nucleon-nucleon collision, at the simplest level, can be viewed as a collision between single partons from each nucleon (Figure 2.1). The partons that will participate in the hard scattering from each nucleon, as well as the momentum fraction they carry, are chosen from known parton distributions. PYTHIA contains a library of available distributions ranging from leading order to more complex models for the low-x behaviour of gluons.

The final state partons resulting from the hard scattering, as well as their momenta, are determined by Monte Carlo simulation of pQCD differential cross sections.

### 2.4.2 Radiation

The initial state. space-like partons ($E^2$ - $p^2$ < 0) have a chance to radiate other partons before scattering takes place. The probability and momentum distribution of initial state radiation are determined by the DGLAP equations [15] (refer back to Sec. 2.3 for more detail). but a coding process named "backward evolution" [20] ensures that energy and momentum are conserved during initial state radiation. The final state. time-like partons ($E^2$ - $p^2$ > 0) might radiate other partons. reducing their energy [21]. The type and kinematics of the radiated parton are also determined by the DGLAP equations.

### 2.4.3 String Formation

After the individual partons have had a hard scattering. the system consists of several components. First. there are the partons that were produced by the scattering. These could be partons produced at the hard scattering point or radiated gluons. Secondly. there are the beam remnants. Since a single quark or gluon was chosen out of each nucleon to actually scatter. the rest of the nucleon remains. This is usually in the form of a diquark. If a u quark is picked out of the nucleon. then there is a ud diquark with net color charge remaining that is color-connected to the hard interaction.

The long-range nature of QCD confines partons. which have a net color charge. into colorless observable states: hadrons. This process is not as of yet directly calculable and is. therefore. phenomenologically modeled. The model employed within PYTHIA is based on string fragmentation [22]. which will briefly be discussed in the next section.

The color-charged partons. radiated partons. and beam remnants are connected to form colorless strings. This is done by tracing the color flow information from the initial participating partons through the interaction [23]. Each QCD process might have several color flow possibilities. For example in same quark elastic scattering ($qq \rightarrow qq$) there are two possible color flow situations because there are two contributing diagrams, a t-channel and u-channel diagram. Whereas in different quark scattering ($qq' \rightarrow qq'$) there is only one diagram and therefore only one possible color flow configuration.

### 2.4.4 String Fragmentation/Hadronic Decay

Once the strings are formed, JETSET fragments them into stable and unstable hadrons according to the Lund fragmentation scheme [22]. For example, the fragmentation process for a simple $q\bar{q}$ system proceeds by breaking the string at different points from each end, consequently forming different $q\bar{q}$ pairs that become mesons. Any unstable hadrons produced during string fragmentation decay further, usually using an isotropic distribution for the momenta of the decay products, into stable particles that can be compared to particles that appear in experimental detectors.

### 2.4.5 Sample Program and Output from PYTHIA/JETSET

PYTHIA and JETSET are built as slave systems used by a master program. The master program defines the parameters of the collision and calls subroutines within PYTHIA or JETSET to perform specific tasks. This greatly simplifies the use of PYTHIA/JETSET, as many routines are not called directly by the user. Some common routines that can be called in a master program are **pyinit**, **pyevnt**, **luexec**, and **lueevt**.

To give a better perspective on how PYTHIA/JETSET simulates collisions, a sample program and a portion of it's available output is displayed in Figure 2.4 and 2.5. This section will contain detailed explanations of various components of the program and accompanying table. The fortran program displayed in Figure 2.4 simulates collisions between two protons, in their center-of-momentum frame, with $\sqrt{s} = 40\ GeV$ using PYTHIA/JETSET routines. This particular simulation only models one particular type of inelastic collision between protons: one in which quarks are chosen from each proton and scatter elastically (`msub = 11`). If the simulation was run with the full range of possible QCD processes, including elastic and diffractive events, the resulting overall cross section calculated by PYTHIA/JETSET would be the total cross section for proton-proton scattering at 40 $GeV$.

In addition to defining the initial state, the final state can be tailored to certain specifications. Within this sample program, all species of pions and rhos that have decay channels within JETSET are prevented from decaying within each event. This is achieved for the neutral pion by `mdcy(lucomp(111),1) = 0` (line 14). The collisions initial configuration is entered into PYTHIA by calling the `pyinit` subroutine, events are generated by calling `pyevnt`, and a table containing various details of each event is generated by calling the `lulist(1)` subroutine.

The kinematic information about the final state formed during an event can be accessed through arrays defined in the `LUJETS` common block. Lines 17-20 in the program run through all of the particles involved in each event, pick out particles appearing in the final state, and print out the particle type's code and energy.

Figure 2.5 displays output from the sample program previously described. This table was created by calling the `LULIST(1)` subroutine and gives a general description of each event generated. The individual lines contain various information about each particle involved in the simulation. For example, the column labeled `particle/jet` gives the particle type, the column labeled `KF` gives the numeric code of each particle type used within PYTHIA/JETSET, and the last four columns give momentum.

energy. and mass information for each particle/jet.

The event listing is somewhat sequential: lines 1 and 2 describe the intial state protons and lines 3 and 4 refer to the partons involved in the hard scattering process. Since no initial state radiation occurred in this event. the following two lines describe the same u-quarks in lines 3 and 4. Scattering is performed and descriptions of the final state u-quarks appear in lines 7 and 8 with momenta determined by Monte-Carlo simulation of the differential cross section for elastic quark scattering.

Lines 9-13 refer to the entire system after the hard scattering has taken place and consists of the final state quarks resulting from the hard scattering. any gluons from final (initial) state radiation. and the beam remnants from each proton. Because u-quarks have participated in the hard process. the beam remnant is a ud diquark in color charged state. The u-quark and gluon in lines 11 and 12 both have an entry of 8 in the column labeled `orig`. This indicates that the gluon appeared during final state radiation off of the produced u-quark in line 8.

The next step in event generation is the formation of strings from the produced partonic and remnant system. Lines 9-10 and 11-13 are connected to form two separate strings. The strings of lines 14 and 22 are then fragmented into hadrons. The final state hadrons. after all produced unstable hadrons have decayed. have an entry of 1 in the column labeled `KS` to indicate that these particles can be observed in the final state.

### 2.4.6 Leptonic Decay Modes

In the fifth chapter. an investigation into dileptons from various decays is made. One such decay that is available in JETSET is the Dalitz decay of the $\pi^0 \rightarrow \gamma e^+ e^-$. The decay width of this process is calculable. This allows JETSET to Monte Carlo the invariant mass distribution of the $e^+e^-$ pair as well as the kinematics of the $\gamma, e^+, e^-$. The dilepton channel is not the only possible decay channel for $\pi^0$. The dominant channel is $\pi^0 \rightarrow \gamma\gamma$ with a branching fraction of 98%. Since these branchings are known, JETSET can statistically choose which decay channel will be taken.

As seen in the branching ratio for $\pi^0 \rightarrow \gamma e^+e^-$, the fraction for processes resulting in dileptons are on average quite small. Therefore, not much of the overall physics is missed by excluding them. At present, JETSET does not include all of the dilepton channels necessary for the study described later in this thesis. These decays are $\eta' \rightarrow \gamma e^+e^-$, $\omega \rightarrow \pi^0 e^+e^-$, $a_1 \rightarrow \pi e^+e^-$, $\omega \rightarrow e^+e^-$, and $\rho \rightarrow e^+e^-$. Since the Dalitz type decays are calculable, we added them to JETSET in a similar manner to $\pi^0$ dilepton decay. This was done by using the differential decay width to Monte Carlo the invariant mass of the dilepton pair and full squared matrix element to Monte Carlo the angular distribution. The invariant mass distribution for the decay width of $\omega \rightarrow \pi^0 e^+e^-$ is displayed in the following equation:

$$\frac{1}{\Gamma}\frac{d\Gamma}{dM^2} = \frac{\alpha}{3\pi M^2}\frac{((m_\omega{}^2 - m_\pi{}^2 - M^2)^2 - 4M^2 m_\pi{}^2)^{3/2})}{(m_\omega{}^2 - m_\pi{}^2)^3} \qquad (2.24)$$

where $M = (p_{e^+} + p_{e^-})^2$ is the invariant mass of the electron-positron pair. For $\omega$ decay events generated by JETSET. Figure 2.6 displays a plot of this distribution and Figure 2.7 shows the rapidity spectrum for the same $e^+e^-$ pairs. The shape of both distributions are as expected; the invariant mass spectrum fall off roughly as an inverse power of the invariant mass and the rapidity distribution is symmetric around the rapidity of the $\omega$.

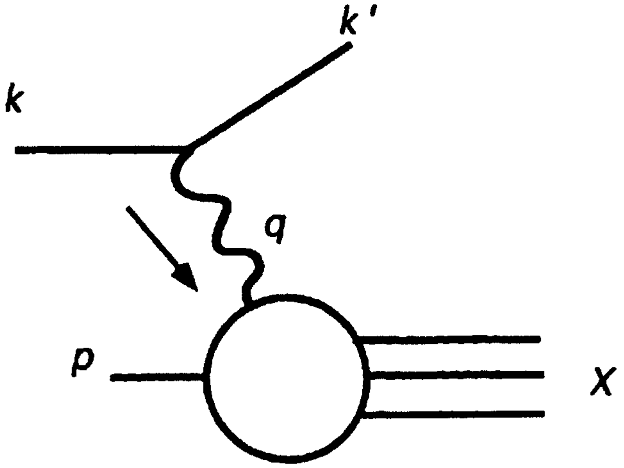

Figure 2.1: Schematic for deep inelastic scattering (DIS) [13].

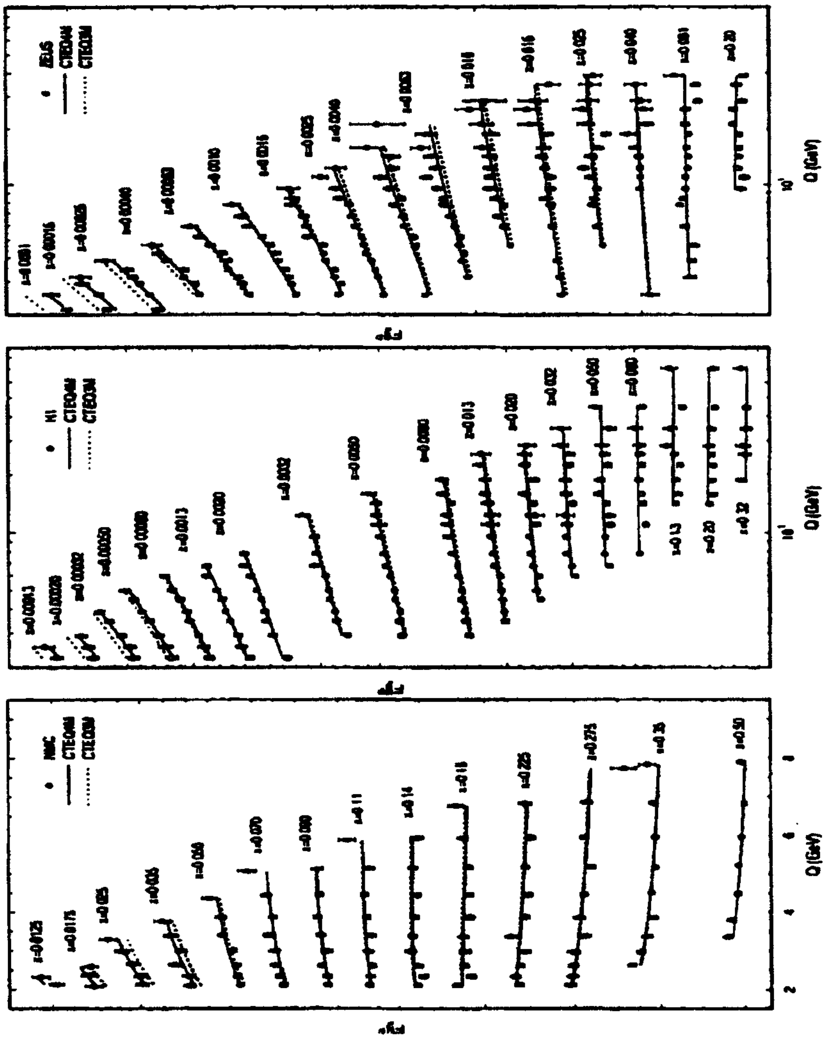

Figure 2.2: Structure functions calculated from NLO pQCD and CTEQ4M distribution functions as compared to data [17].

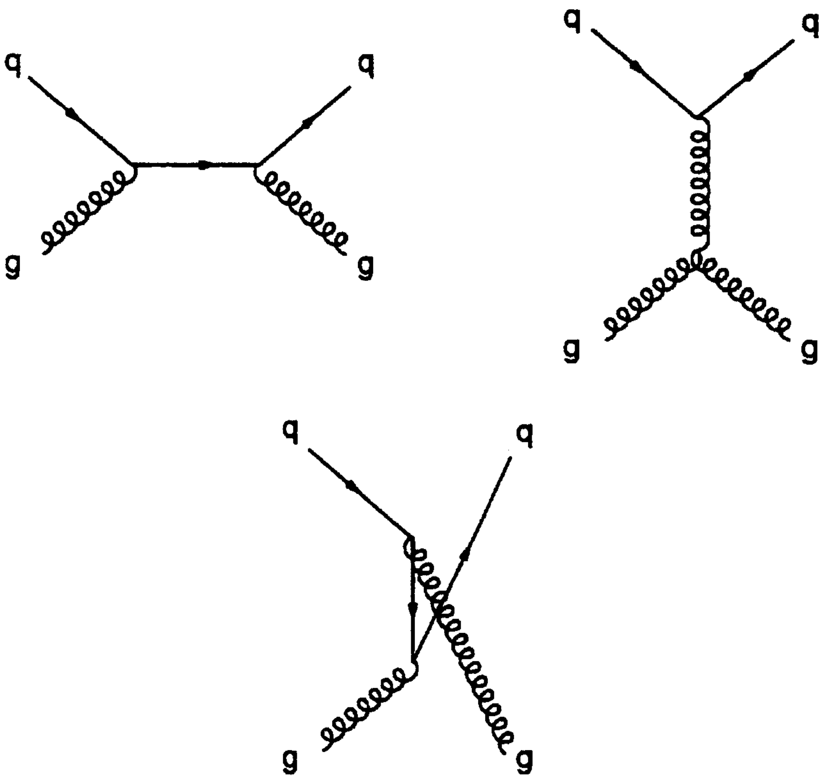

Figure 2.3: Feynman diagrams for $qg \rightarrow qg$.

```
        program ppcoll
c
        double precision mn,rs,p1,p2
        integer nev,iev,n
c     PYTHIA/JETSET common blocks
        COMMON/LUJETS/ N,K(4000,5),P(4000,5),V(4000,5)
        COMMON/LUDAT3/ MDCY(500,3),MDME(2000,2),BRAT(2000),KFDP(2000,5)
        COMMON/PYSUBS/ MSEL,MSUB(200),KFIN(2,-40:40),CKIN(200)
c
c     mass of nucleon, cm energy, and number of events
        mn=0.933
        rs=40.
        nev=10
c     momentum of target and projectile in GeV/c
        p1=sqrt(rs**2-4*mn**2)/2.
        p2=sqrt(rs**2-4*mn**2)/2.
c
        msel=0
c     turns on hard quark scattering only
        msub(11)=1
c     turn off neutral pion decay
14      mdcy(lucomp(111),1)=0
        mdcy(lucomp(113),1)=0
        mdcy(lucomp(213),1)=0
        mdcy(lucomp(-213),1)=0
c     sets up momenta of colliding nucleons
        p(1,1)=0.
        p(1,2)=0.
        p(1,3)=p2
        p(2,1)=0.
        p(2,2)=0.
        p(2,3)=-p1
c     lets pythia know collision is p p with the user defined momenta from
c     above
        call pyinit('user','p','p',rs)
        do 40 iev=1,nev
c     performs scattering, string formation, fragmentation, and subsequent
c     decays
                call pyevnt
                call lulist(1)
17              do 20 j=1,n
18                      if (k(j,1).ne.1) goto 20
19                      print*, k(j,2), p(j,4)
20              continue
40      continue
1000    end
```

Figure 2.4: Sample program that calls PYTHIA/JETSET routines to simulate proton proton collisions at 40 *GeV* center of mass energy.

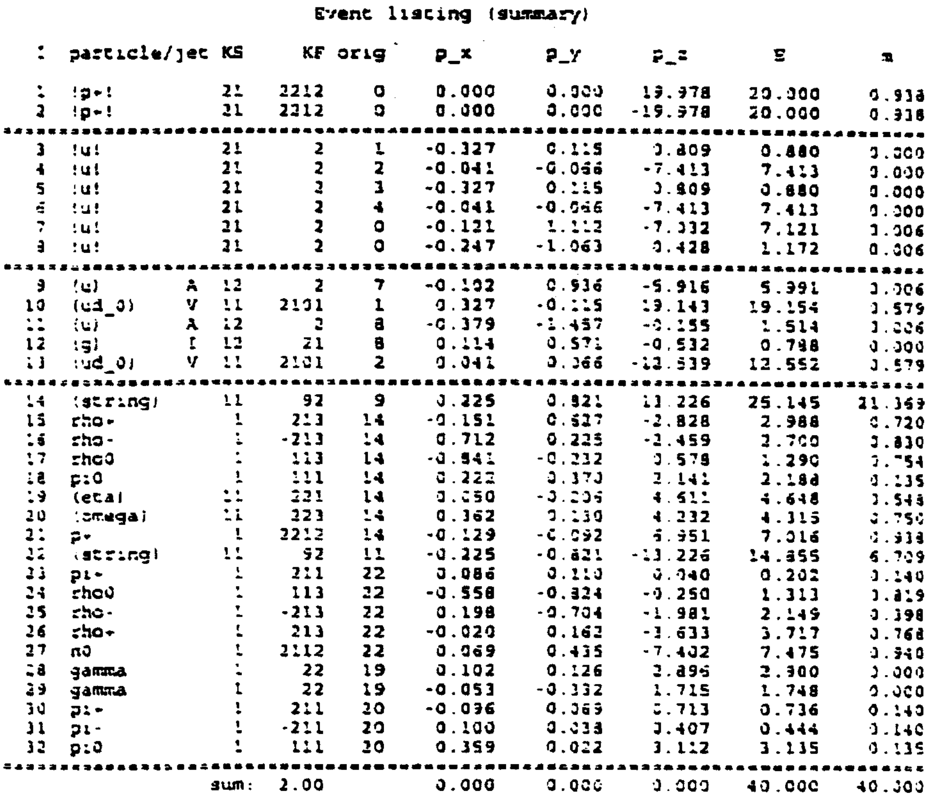

```
                         Event listing (summary)

 I  particle/jet KS     KF orig    p_x      p_y      p_z       E        m

  1  !p+!        21   2212    0    0.000    0.000   19.978   20.000    0.938
  2  !p+!        21   2212    0    0.000    0.000  -19.978   20.000    0.938
==============================================================================
  3  !u!         21      2    1   -0.327    0.115    0.809    0.880    0.000
  4  !u!         21      2    2   -0.041   -0.066   -7.413    7.413    0.000
  5  !u!         21      2    3   -0.327    0.115    0.809    0.880    0.000
  6  !u!         21      2    4   -0.041   -0.066   -7.413    7.413    0.000
  7  !u!         21      2    0   -0.121    1.112   -7.032    7.121    0.006
  8  !u!         21      2    0   -0.247   -1.063    0.428    1.172    0.006
==============================================================================
  9  (u)       A 12      2    7   -0.102    0.936   -5.916    5.991    0.006
 10  (ud_0)    V 11   2101    1    0.327   -0.115   19.143   19.154    0.579
 11  (u)       A 12      2    8   -0.379   -1.457   -0.155    1.514    0.006
 12  (g)       I 12     21    8    0.114    0.571   -0.532    0.788    0.000
 13  (ud_0)    V 11   2101    2    0.041    0.066  -12.539   12.552    0.579
==============================================================================
 14  (string)    11     92    9    0.225    0.821   11.226   25.145   21.369
 15  rho+         1    213   14   -0.151    0.527   -2.828    2.988    0.720
 16  rho-         1   -213   14    0.712    0.225   -2.459    2.700    0.830
 17  rho0         1    113   14   -0.841   -0.232    0.578    1.290    0.754
 18  pi0          1    111   14    0.222    0.370    2.141    2.188    0.135
 19  (eta)       11    221   14    0.050   -0.206    4.611    4.648    0.549
 20  (omega)     11    223   14    0.362    0.130    4.232    4.315    0.750
 21  p+           1   2212   14   -0.129   -0.092    6.951    7.016    0.938
 22  (string)    11     92   11   -0.225   -0.821  -11.226   14.855    6.709
 23  pi+          1    211   22    0.086    0.110    0.040    0.202    0.140
 24  rho0         1    113   22   -0.558   -0.324   -0.250    1.313    0.819
 25  rho-         1   -213   22    0.198   -0.704   -1.981    2.149    0.398
 26  rho+         1    213   22   -0.020    0.162   -3.633    3.717    0.768
 27  n0           1   2112   22    0.069    0.435   -7.402    7.475    0.940
 28  gamma        1     22   19    0.102    0.126    2.896    2.900    0.000
 29  gamma        1     22   19   -0.053   -0.332    1.715    1.748    0.000
 30  pi+          1    211   20   -0.096    0.069    0.713    0.736    0.140
 31  pi-          1   -211   20    0.100    0.038    0.407    0.444    0.140
 32  pi0          1    111   20    0.359    0.022    3.112    3.135    0.135
==============================================================================
                 sum:   2.00           0.000    0.000    0.000   40.000   40.000
```

Figure 2.5: LULIST(1) output from sample program.

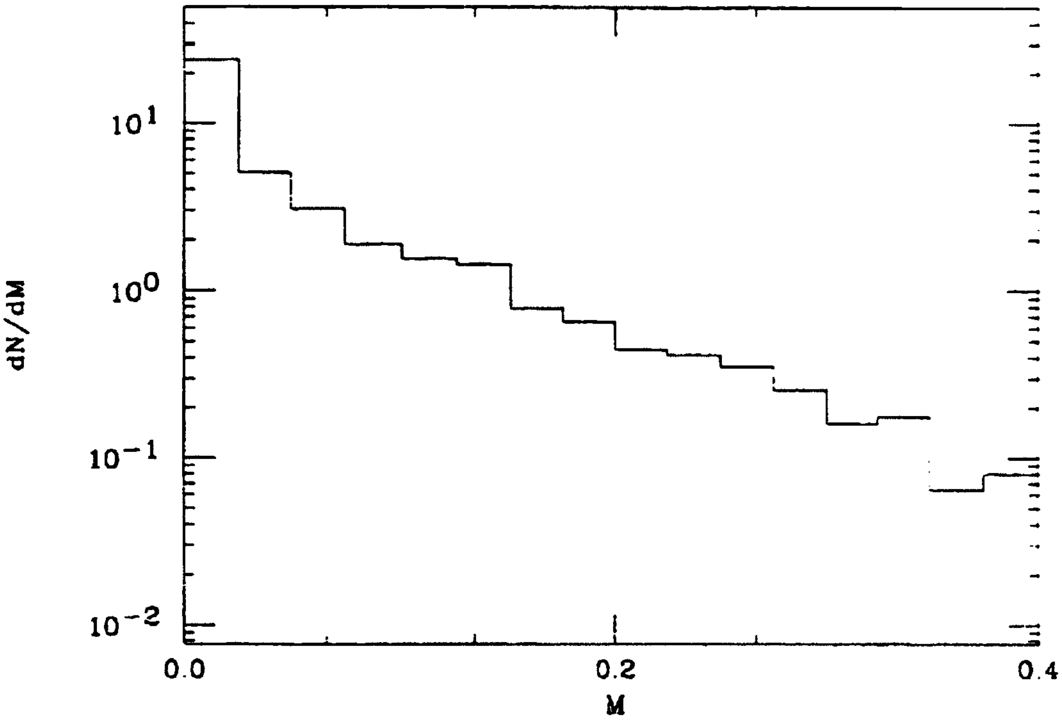

Figure 2.6: Invariant mass distribution of lepton pairs in $\omega \rightarrow \pi e^+e^-$.

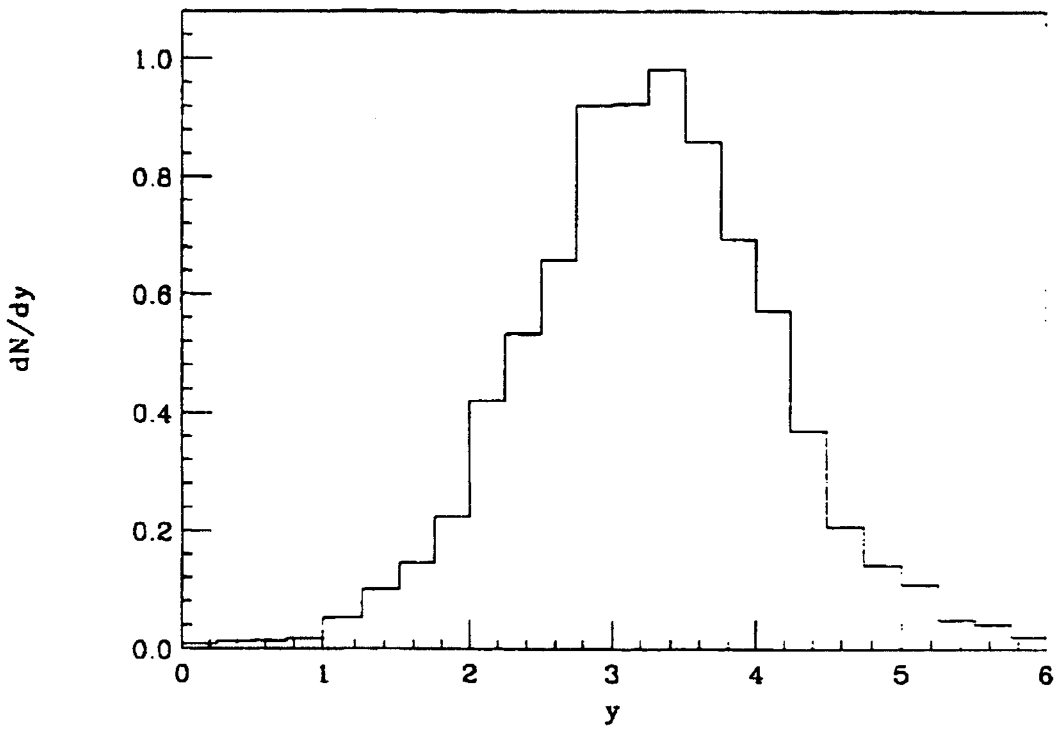

Figure 2.7: Rapidity distribution of electrons and positrons resulting from $\omega \rightarrow \pi e^+ e^-$.

# Chapter 3

# Parton Cascades

## 3.1 Introduction

In order to model a relativistic heavy ion collision in which a quark-gluon plasma is formed. simulations are needed that include free partons at the intial. prethermalized stage of the collision. Ideally. this model could be used to study possible signatures for QGP formation. Parton cascades are this type of model.

A parton cascade is based on the following premise: when nuclei are scattered at ultra-relativistic energies. they can be viewed as an ensemble of freely moving partons that scatter with cross sections determined by perturbative QCD. Figure 3.1. With this basis. the partons are given momentum fractions of the momentum per nucleon. chosen from parton distributions for nucleons. and propagate in time according to classical trajectories. Scatterings between partons occur based on the spatial separation of partons and cross sections for parton reactions. The kinematics of the final state are Monte-Carlo chosen with pQCD squared matrix elements. New partons are added to and subtracted from the population by radiation and absorption. A description of partonic radiation is calculable perturbatively. Absorption can be viewed as the time-reversed process of radiation so that detailed balance can provide cross sections. The partons continue to interact and propagate in time until until scattering energies fall below the perturbative cut-off. At this point the partons are combined into detectable hadrons.

The question addressed is whether space-time development of partons can be treated in a classical manner, particularly whether propagation of off-shell partons is either justified or reasonable. Since most partons at mid-rapidity in a high-energy collision are the result of Bremsstrahlung-like diagrams, understanding the space-time coordinates at which they appear is essential to making a meaningful simulation. This importance is amplified by the fact that the incoming nuclei are Lorentz contracted to a few tenths of a fermi, and that the creation times might be additionally enhanced by relativistic $\gamma$ factors. Thus, the space-time extent which arises from the decay time of partons can easily be greater than the actual longitudinal size of incoming nuclei.

Space-time issues do not arise in usual perturbative QCD as calculations are performed in momentum space. Standard momentum-space Monte-Carlo methods exist for simulating the branching of both the incoming and outgoing states, including Bremsstrahlung [20]. Modeling processes where rescattering becomes important, such as $J/\psi$ suppression and the Landau-Pomeranchuk effect indeed requires space-time variables. Although many of these analyses are based on classical pictures, quantum mechanical treatments of such phenomena do exist and the lessons learned from such studies should help illuminate solutions to the problems discussed in this section [27].

For lower-energy heavy ion collisions, where nucleons, pions and delta resonances are the dominant particles, classical descriptions are well justified and have been successful phenomenologically. An example of a collision where off-shell particles would be incorporated is in the formation of a pion from nucleon-nucleon scattering. Two nucleons can collide, forming a nucleon and a delta. The delta's mass would be chosen with a width consistent with its lifetime $\tau$ . The delta would then propagate on a straight-line trajectory with a probability of decaying during any time step of $\delta t/(\gamma\tau)$. The factor $\gamma$ accounts for the time dilation of the moving delta resonance. The cross section for the inverse process, where a pion merges with a nucleon to form a delta, is determined by time reversal or detailed balance arguments. If the pion-creation process was handled quantum mechanically, one would calculate amplitudes for the pion to be emitted from the outgoing legs of both nucleons, for either could have been a delta. The two amplitudes would then be added coherently, then squared to yield the total cross section for two nucleons to make a pion.

In a parton cascade the most common reaction one would model would entail two partons colliding to produce three or more partons. In a parton cascade picture this is modeled sequentially, ignoring the interference of various paths. First a collision is chosen which would result in two outgoing partons, both with an effective off-shell mass. The partons would then decay statistically, creating an additional parton at each branching.

By considering the most simple process, the annihilation of an $e^+e^-$ pair into three partons, the results for a classical sequential picture such as is used in a parton cascade are compared to results obtained from a correct perturbative treatment which includes all interference effects. In the next section problems associated with the massless nature of most partons are discussed, and in the subsequent section the additional problems that arise when one of the outgoing partons is a gauge boson are outlined. The importance of these issues as well as other problems with parton cascades are detailed in the conclusion.

## 3.2 Massless Partons

To illustrate the problems within a cascade associated with the massless nature of partons, an elementary Bremsstrahlung process is considered, where a vector boson decays into a quark-antiquark pair, with the quark radiating a scalar particle. The case of radiating a scalar rather than a vector particle is considered because it allows us to neglect, until the next section, complications associated with gauge theories. It will be shown that the distribution of final momenta is inconsistent with a picture where the scalar was formed solely through the decay of an off-shell quark.

The inconsistency arises from the fact that the complete amplitude includes equally important contributions from two different processes. The time ordered processes and their relationship to the single Feynman diagram is depicted in Figure 3.2 where a, b, c, d, and e represent the virtual photon, final state anti-quark, intermediate quark (anti-quark), final state scalar particle, and the final state quark, respectively.

The first time ordered process is the actual decay of the vector boson into a quark anti-quark pair where the quark later radiates the scalar particle. The second process depicts the scalar and a quark anti-quark pair being spontaneously emitted from the vacuum. The virtual photon is absorbed by the anti-quark at a later time, leaving the three particles on-shell. In the first process, the $\gamma^* q\bar{q}$ vertex occurs before the $q\phi q$ vertex; and in the second process, the $q\phi q$ vertex occurs before the $\gamma^* q\bar{q}$ vertex.

As far as the final observable is concerned, it does not matter if the $\gamma^* q\bar{q}$ vertex occurs at an earlier time than the $q\phi q$ vertex or vice versa, because the final state is the same in either case. This behavior can be seen through the definition of a propagator. A propagator is defined as a vacuum expectation value of the time ordered product of relevant fields. [28].

$$\Delta_F(x-y) = \langle 0|T[\psi(x)\psi^\dagger(y)]|0\rangle = \langle 0|\psi(x)\psi^\dagger(y)|0\rangle\theta(x_0-y_0)+\langle 0|\psi(y)\psi^\dagger(x)|0\rangle\theta(y_0-x_0) \tag{3.1}$$

where $x^\mu$ and $y^\mu$ are four vectors representing the space-time information of each vertex.

This study considers a theory where the vector boson decays into a quark and antiquark of possibly different flavors and where the scalar couples only to the quark. not to the antiquark. In this model. the amplitude can be described by only one Feynman diagram. Thus. complications due to the different time orderings. isolated from difficulties associated with other kinds of interference can be investigated.

The amplitude for the process $\gamma^* \to q\bar q\phi$ is

$$\mathcal{M} = g_e g_{\text{scalar}}\bar u(p_e)(\not p_d + \not p_e)\gamma^\mu v(p_b)\epsilon_\mu/t \tag{3.2}$$

and the amplitude squared and summed over polarization is

$$\sum|\mathcal{M}|^2 = 4g_e^2 g_{\text{scalar}}^2 s/t \tag{3.3}$$

where $s = 2p_b \cdot p_d$ and $t$. the invariant mass squared of the off-shell quark. $= 2p_d \cdot p_e$. Multiplying by the appropriate factors yields the cross section.

$$\frac{1}{\sigma_0}\frac{d\sigma}{dz\,d\hat t} = \frac{\alpha_{\text{scalar}}}{3\pi}\frac{(1-z)(1-\hat t)^2}{\hat t} \tag{3.4}$$

where $z$ is a light cone variable defined as $(E + p_z)_e/\sqrt{t}$ and $\hat t = t/Q^2$. with $Q$ being the off-shell mass of the decaying vector particle. so that

$$s = (1-z)(1-\hat t) \tag{3.5}$$

If the cross section is evaluated in the rest frame of the virtual quark. $z$ can be written in terms of the angle between the quark and anti-quark: $z = (1+\cos\theta)/2 =$

$\cos^2(\theta/2)$. The cross section then becomes solely a function of the off-shell mass of the virtual quark and the angle.

$$\frac{1}{\sigma_0}\frac{d\sigma}{d\cos\theta d\hat{t}} = \frac{\alpha_{\text{scalar}}}{6\pi}\frac{(1-\hat{t})^2 sin^2(\theta/2)}{\hat{t}} \tag{3.6}$$

By inspecting the Feynman diagram, one might be tempted to interpret Equation (3.6) as the probability that a virtual quark, with invariant mass squared $t$, decays into an on-shell quark and scalar. This interpretation is incorrect, because parity conservation demands that the decay of a spin one-half particle should be isotropic in the frame of the off-shell quark. The actual physical interpretation is not clear because the cross section is a consequence of interference between the two different time orderings in Figure 3.2. The first time ordering is the actual decay, but the presence of the second time ordering results in the $\cos\theta$ dependence.

In order for the interference between time ordered diagrams to be significant, both time ordered diagrams must contribute equally to the single Feynman diagram. To see this, refer again to Figure 3.2. To investigate the contribution of each diagram, consider the off-shellness of the intermediate state in its own rest frame. Assuming that the intermediate quark has an on-shell mass that is comparable in magnitude to the kinetic energy of the outgoing particles, the intermediate quark in the first diagram has an off-shellness,

$$\Delta E_1 = E_d + E_e - m_c \tag{3.7}$$

and the intermediate quark in the second scenario has

$$\Delta E_2 = -E_d - E_e - m_c \tag{3.8}$$

With this condition on m$_c$, the diagram that describes the actual decay is less off-shell than the situation described by the second diagram, $\Delta E_1 < \Delta E_2$. This means that the actual decay will be the dominant contribution to the Feynman diagram. But if partons are massless, then both situations are off-shell by the same amount ($\Delta E_1 = \Delta E_2$) and contribute equally to the amplitude. It is exactly the interference between the two time orderings that causes the $\cos\theta$ dependence in the cross section. Even in a non-gauge theory, the process $\gamma^* \rightarrow q\bar{q}\phi$ cannot be interpreted as a the decay of a virtual quark with invariant mass $\sqrt{t}$ into an onshell quark and scalar.

When classically modeling a one-to-three process as described above, one would be tempted to simulate the creation of the anti-quark pair statistically choosing the off-shell mass of the quark. One would then decay the off-shell quark according to its lifetime. In this way, one has only to simulate two-to-two scatterings, one-to-two decays, and two-to-one fusions in a parton cascade. However, the momentum distribution of the final state will be inconsistent with the full Feynman amplitudes. In addition, fluctuations in the vacuum become very important because scattering off of the vacuum (second time ordering) and the real-time decay (first time ordering) are equally important. Since the structure of the vacuum is non-perturbative, scattering off vacuum fluctuations might be ill-treated in perturbative analogies.

More importantly, this exercise demonstrates that the radiated particle has equal probability of being emitted before the disappearance of the vector boson as after. This implies that particles created in a collision have equal probability of appearing before the collision as after. This is true even when considering only Bremsstrahlung off outgoing lines in the Feynman diagram.

Understanding this is crucial, because the energy density is greatly affected by the timing of particle production. If the particles are all produced instantaneously, the density will be higher and if they are produced at some later time proportional to the decay time the energy density may be too low. Therefore, correctly implementing this feature within the parton cascade is essential.

## 3.3 Gauge Nature of Gluons

In addition to the problems due to masslessness discussed in the previous section, even more severe complications arise from the gauge nature of gluons. To illustrate such problems, the decay of a virtual photon into a quark-antiquark pair is considered, where a gluon is radiated off one of the quark legs as in Figure 3.3.

A certain amount of $z$-dependence in the cross section is expected because the partons are massless, but in this section it will become apparent that the $z$-dependence that arises has a divergence in $1/(1-z)$ and is due to classical radiation of the gluon from the accelerated quark and anti-quark pair.

To see where the $z$ dependence occurs, one needs to look at the direct terms squared and summed over polarization as well as the interference term. Since only the sum of these terms is gauge invariant, a gauge needs to be chosen. Using the labelling scheme illustrated in Figure 3.3, the calculation is performed in an axial gauge defined by the rest frame of the virtual photon, $n \cdot A = 0$ or $n^\mu = Q^\mu$.

The direct and interference terms become,

$$\sum |\mathcal{M}_1|^2 \propto \frac{(1-z)(1-\hat{t})(1+z^2(1-\hat{t})^2)}{\hat{t}(1-z(1-\hat{t}))^2} \tag{3.9}$$

$$\sum |\mathcal{M}_2|^2 \propto \frac{\hat{t}(1+z^2(1-\hat{t})^2)}{(1-z)(1-\hat{t})(1-z(1-\hat{t}))^2} \tag{3.10}$$

$$\sum |\mathcal{M}_1^\dagger \mathcal{M}_2| + |\mathcal{M}_2^\dagger \mathcal{M}_1| \propto \frac{z(1-\hat{t})}{(1-z(1-\hat{t}))^2} \tag{3.11}$$

where $\hat{t}$ and $z$ are invariantly defined as $\hat{t} = t/Q^2$, $z = (E+p_z)_2/(E+p_z)_{\gamma^*}$, and $Q$ is the invariant mass of the virtual photon. In the leading pole approximation ($\hat{t} \to 0$), the familiar splitting function is recovered,

$$\frac{1}{\sigma_0}\frac{d\sigma}{dz\,d\hat{t}} = \frac{2\alpha_s}{3\pi}\frac{1+z^2}{(1-z)\hat{t}} = \frac{\alpha_s}{2\pi\hat{t}}P_{q\rightarrow qg}(z) \qquad (3.12)$$

All three terms have a pole in $(1-z)$. If one were to consider the process as a decay of a virtual quark, the decay would be divergent anisotropically in the rest frame of the virtual quark, with the gluon going backward and the quark forward. The $(1-z)$ poles can be interpreted as preferences for emitting low energy gluons with arbitrary orientations or gluons that are collinear with either the quark or anti-quark. This $z$-dependence dominates the behaviour of the final state partons. As a consequence, it is much more serious than the $z$-dependence found in the previous section which was a result of the equal strength interference between the decay and scattering off of the vacuum.

In the limit that the gluon is soft, the light cone variables can be rewritten in terms of the gluon energy $\omega$, and the angle $\theta$ between the final state gluon's and virtual quark's momenta: $(1-z) = \omega(1+\cos\theta)/2Q$, $\hat{t} = \omega(1-\cos\theta)/2Q$, and $dz\,d\hat{t} = \omega d\omega d\cos\theta/2Q^2$. The rate then becomes

$$\lim_{\omega\rightarrow 0}\frac{1}{\sigma_0}\frac{d\sigma}{d\omega d\cos\theta} = \frac{4\alpha_s}{3\pi}\frac{1}{\omega sin^2\theta} \qquad (3.13)$$

The same behaviour can be found in classical radiation from accelerating charges. The energy and angular distribution of radiation from oppositely charged particles moving back to back,

$$\lim_{\omega\rightarrow 0}\frac{dN}{d\omega d\cos\theta} = \frac{2e^2\beta^2}{\pi}\frac{1}{\omega sin^2\theta} \qquad (3.14)$$

contains the same poles in the energy spectrum of radiation as well as the angle between the accelerating charge and the point where the radiation was observed. With this insight, the low energy characteristics of the rate for $\gamma^* \rightarrow q\bar{q}g$ can be attributed to radiation from accelerating the color "charge" of the quark anti-quark pair.

To emphasize this point further, consider the same calculation in an axial gauge defined by the rest frame of the virtual quark, $n^\mu = p_2^\mu + p_3^\mu$. The individual terms become,

$$\sum |\mathcal{M}_1|^2 \propto \frac{(1-z)(1-\hat{t})}{\hat{t}} \tag{3.15}$$

$$\sum |\mathcal{M}_2|^2 \propto \frac{\hat{t}^2 + 2z(1-\hat{t})(1-(1-z)(1-\hat{t}))}{\hat{t}(1-z)(1-\hat{t})} \tag{3.16}$$

$$\sum |\mathcal{M}_1^\dagger \mathcal{M}_2| \propto \frac{z(1-\hat{t})}{\hat{t}} \tag{3.17}$$

In this gauge, only the direct term where the gluon is radiated from the anti-quark has a $(1-z)$ divergence; whereas in the previous gauge all of the terms contain a $(1-z)$ pole. Both results are consistent with classical radiation. In the rest frame of the virtual quark, only the anti-quark is accelerated and can radiate color "charge" quanta; whereas the previous gauge was only "physical" in a frame where both the quark and anti-quark were accelerated.

In the previous section, it was shown that there was no pole in $(1-z)$. Why didn't the scalar case radiate due to acceleration of the quark? This is because there is no scalar charge for massless particles, $\bar{u}(p)u(p) = m/E = 0$.

## 3.4 More Problems with Parton Cascades

In addition to the difficulties in correctly modeling the time evolution of partonic radiation within a parton cascade, several other issues need to be addressed..

Within the phenomenology of high energy physics, the initial momenta of an incoming parton is determined by parton distributions [17, 16, 18] which depend on the momentum scale of the scattering. The remaining unscattered partons are assumed to leave the collision without interacting with the scattered partons. Whereas the choice of the momentum scale is obvious in nucleon-nucleon or nucleon-electron collisions. it is not clear what $Q^2$ should be in nucleus-nucleus collisions.

In Geiger's parton cascade [2], a minimum $Q^2$ is chosen so that the number and momentum fractions of the initial partons can be determined from parton distributions for nucleons. A value of $Q^2$ is chosen that is on the order of but smaller than the $\langle Q^2 \rangle$ of individual parton scatterings. Then the partons are allowed to evolve in space-time. When an individual scattering occurs with a momentum scale larger than the $\langle Q^2 \rangle$, the discrepancy is adjusted by emitting more partons in that region using the DGLAP evolution equations [15] and backward evolution [20] in momentum space to insure energy and momentum balance.

To complicate matters further, all partons in a high energy nuclear collision suffer violent collisions which should alter the form of the structure functions used for nucleon-nucleon or nucleon-electron scattering. This issue has been discussed recently [24], but remains unsolved. The production of particles at mid-rapidity with transverse momenta less that 1 $GeV$ depends strongly on the cutoff of the structure functions at low $x$ which otherwise diverge as $1/x$. Justified criteria for treating the structure functions at low $x$ do not yet exist. Similar cutoff procedures are used in hadronic transport theories and are motivated by the action of the Pauli-exclusion principle. At least for gluon-gluon scattering, this does not apply.

Within the cascade, the geometric shape of the incoming partons should not necessarily be a simple Lorentz-contracted disk. Since the incoming partons are off-shell, they might exist to some degree outside the nuclei. Only the valence quarks exist inside the Lorentz-contracted disk whereas the partons carrying low momentum fractions exist outside the disk [25]. The partons that are smeared outside the Lorentz-contracted disk are known as wee-partons. Such effects have been incorporated into the model of reference [2], but quantitative details remain speculative.

Another set of problems confronting the development of models regards the violation of causality. such as propagation of superluminary signals. Scatterings are usually incorporated by searching for particles that cross at a finite distance $\sqrt{\sigma/\pi}$ where $\sigma$ is the parton-parton cross section. The violation of causality is particularly troublesome for soft collisions where cross sections are large. The presence of these large cross section lead to information being propagated over large distances in the collision region within one time step. This can result in signal speeds much greater than the speed of light. For a detailed discussion of causality violations and methods for handling them within a parton cascade see [26].

After the partons have scattered many times and the center of mass energies of the collisions fall below the region perturbative QCD is applicable. the partons must be combined to form observable hadrons. Several methods for describing hadronization have been used. To truly follow the examples set by hadron-hadron event generators. one would have to incorporate a method for tracking the color flow from the original partons to the partons created by radiation and scattering. This has not been done at this point as it poses. at least. serious computational problems. Despite this obstacle. hadronization methods have been employed based on spatial clustering of partons and transferring the charge and energy information of the partons to the resulting hadrons. The uncertainty of this method and others like it can be minimized by comparing results obtained for nucleon-nucleon scattering to experiment.

## 3.5 Conclusions

Parton cascades are motivated by the goal of creating a space-time model for the intial stage of relativistic heavy ion collisions including rescattering events. The most fundamental challenge for a cascade is to develop criteria for assigning space-time points for created particles. In this chapter simple Bremsstrahlung processes have been investigated in terms of the classical cascade picture and compared with those of the quantum mechanically correct perturbative approach. The problems with the classical cascade come from interpreting Feynman diagrams too literally. A cascade is tenable when only two-to-two scatterings, two-to-one fusions and one-to-two decays are included in the simulation, because detailed balance must be satisfied in such a way that computation times remain reasonable.

It was shown that the amplitude for decaying a photon into three particles includes several contributions. The three particle final state is a result of three different scenarios: a virtual parton is created and then decays, a vacuum fluctuation absorbs the photon leaving three on-shell partons, and finally the partons produced by the decaying photon radiate classically. By only considering the contributions from the decay of the virtual parton, more than just 2/3 of the relevant physics is missing. In the first section, it was shown that the radiated particle was just as likely to be emitted before the photon interacted as after. Neglecting this could have serious consequences, as many pre-equilibrium characteristics are dependent on when and where the mid-rapidity particles are produced. Even more severe implications could occur from ignoring contributions from classical radiation, because it is more than an equal strength effect, it divergently produces low-energy gluons.

One could imagine including the $z$-dependence in the simulation of a Bremsstrahlung event by decaying the off-shell quark according to the full Feynman amplitudes. Such Monte-Carlo procedures are standard in the literature and include multiple gluon emission. The $z$-dependence reflects a $\cos\theta$ dependence, where $\theta$ is the direction of the final state quark as compared to the direction of the anti-quark and is defined in the rest frame of the decaying quark. Thus the decaying quark would need to carry information about the anti-quark with which it was created. Such knowledge of its past would require that the time reversed process has knowledge of its future. Such considerations would violate the classical nature of the cascade while omitting them would sacrifice detailed balance.

One of the issues one would wish to explore with a simulation is whether the excess of low $p_t$ gluons with respect to low $p_t$ quarks remains after the reaction has proceeded for a long time [2, 29], as well as other methods of producing mid-rapidity gluons [58]. Of course when and where the gluons are produced contributes greatly to bulk phenomena such as stopping and chemical potential. Any production mechanism that does not have a space-time component will not effectively model the situation. Until such models include justified space-time prescriptions and formally satisfy detailed balance, conclusions regarding such issues remain dubious.

Alternate approaches to calculating the evolution of the early stage of a relativistic heavy ion reaction have appeared in the literature. McLerran and Venugopalan have studied the treatment of gluon radiation with a Weizsacker-Williams approach [31]. In a hadronic context, Siemens has explored solving the evolution of two and three-point functions [32]. Finally, even if theoretical efforts completely fail, experiment may be able to extract the necessary information about the initial stage through dilepton measurements, extrapolations from $p\bar{p}$ and $pA$ collisions, and inferences from measurements of the final state.

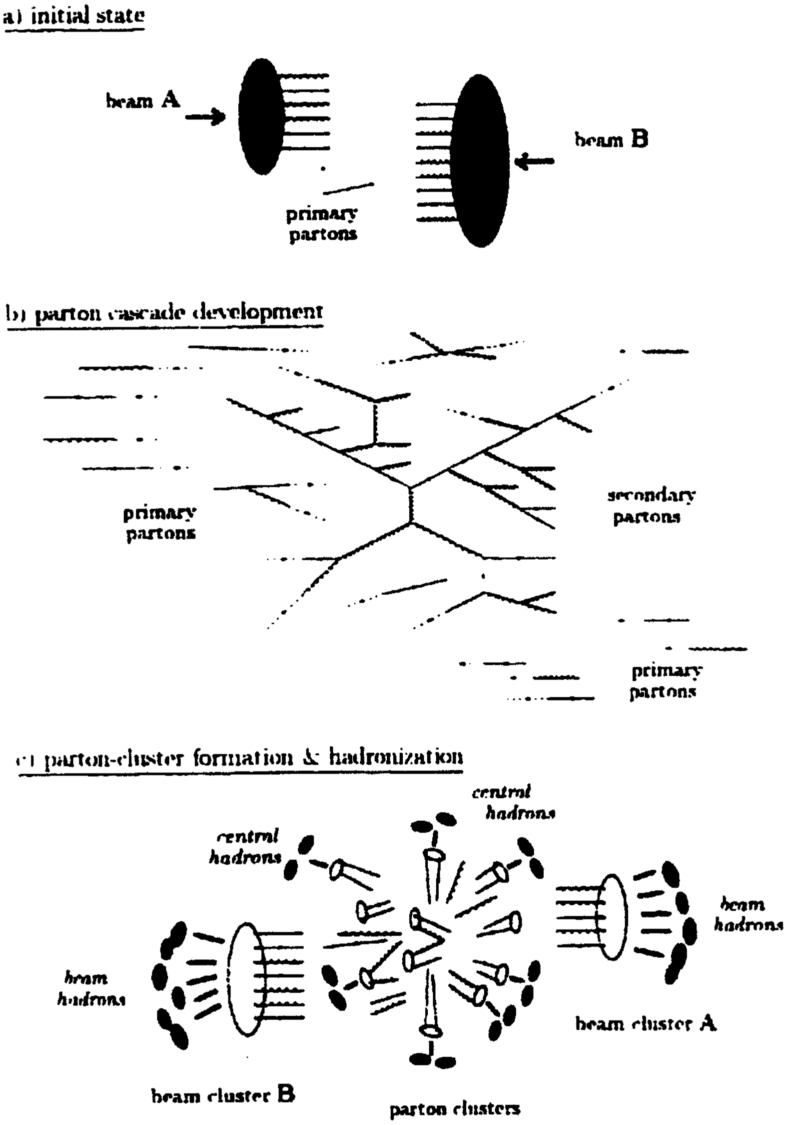

Figure 3.1: Schematic picture for parton cascade [2].

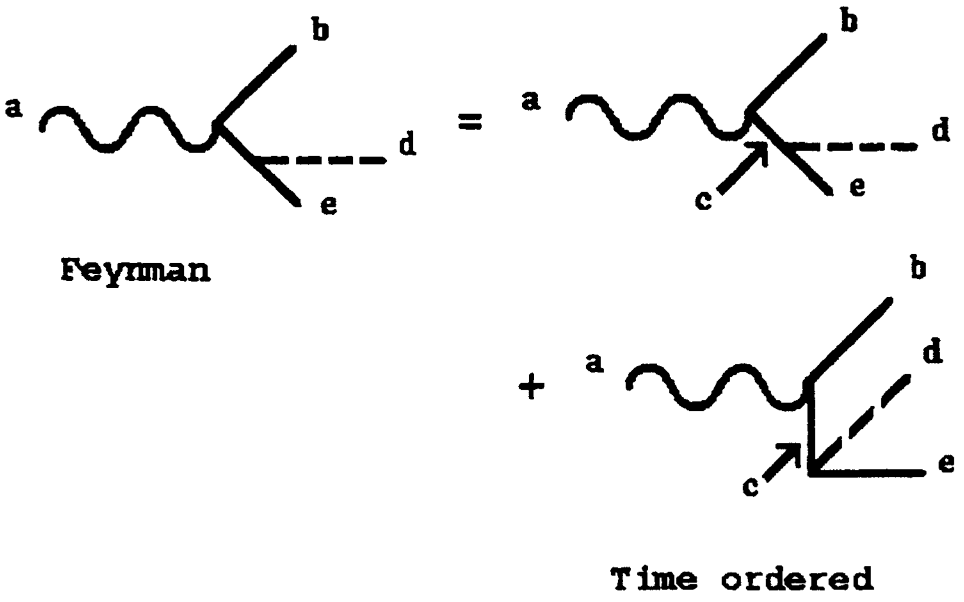

Figure 3.2: Feynman diagram and time ordered equivalent.

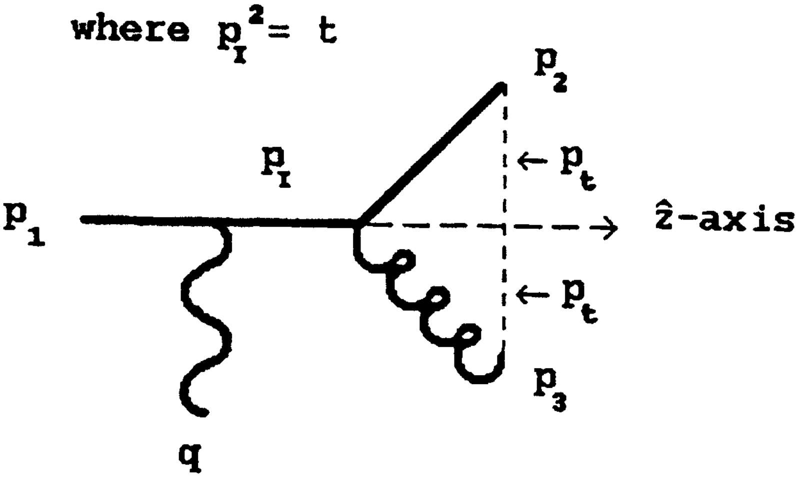

Figure 3.3: Rest frame of virtual photon.

# Chapter 4

# Primary Scattering

## 4.1 Introduction

This chapter will present a basic description of the computer model used in the analysis detailed in the following chapters. Once the simulation's description is complete, comparisons to experimental data for several hadronic observables are shown with varying systems and energies.

The model was developed to simulate ultra-relativistic heavy ion collisions without assuming quark-gluon plasma formation but still incorporating perturbative QCD. Therefore, results from this simulation would serve as background for the parton cascade model described in the previous chapter where an assumption of plasma formation was made. It is based on the simple premise that a heavy ion collision behaves as the superposition of nucleon-nucleon collisions. The number of nucleon-nucleon collisions that occur in one nucleus-nucleus collision can be estimated using Glauber-type geometry. The nucleon interactions, at the energies considered, are characterized by th parton model and perturbative QCD. The use of pQCD nucleon interactions and Glauber geometry to scale from nucleon collisions up to nucleus collisions was motivated by HIJING [4]. Both models have similar foundations, but the model detailed in this thesis extends beyond HIJING to include secondary scattering effects. The resulting model is a relativistic heavy-ion event generator capable of colliding p+A and A+A from roughly 10 $GeV$/nucleon up to several 1000 $GeV$/nucleon in center of mass energy. This energy range encompasses a vast amount of available experimental data as well as data which has yet to be taken.

## 4.2 Model Outline

- *Initialization of nucleons inside nuclei:* The nucleons are positioned randomly inside each nucleus according to the size of the nucleus , $R = 1.1A^{1/3}$. They are given random Fermi momentum in the $x$-$y$ plane and are given $z$-momentum according to the lab energy (or center of mass energy, $\sqrt{s}$).

- *Number of collisions:* The number of collisions is determined geometrically [33]. This calculation is done with the assumption that when a projectile nucleon collides with a target nucleon, it is not entirely destroyed by this collision and is able to also collide with the other target nucleons behind the original one. With this in mind, the number of collisions is then dependent on the density of nucleons and the cross section for a nucleon-nucleon interaction. Within the model used, the density of nuclear matter is taken to be 0.16 nucleons/$fm^3$ and the nucleon total cross section is 40 $mb$. Based on previous work [33], a numerical prescription was developed for calculating this number.

  For a proton-nucleus collision,

$$n(b) = \sigma_{NN} \int dx\, dy\, dz\, \rho(\sqrt{b^2 + z^2}) \tag{4.1}$$

  For nucleus-nucleus collisions,

$$N(b) = \sigma_{NN} \int dx\, dy\, dz_1\, dz_2\, \rho_A(\sqrt{x^2 + y^2 + z_1{}^2})\, \rho_B(\sqrt{x^2 + (y-b)^2 + z_2{}^2}) \tag{4.2}$$

The calculation is slightly different depending on the reference frame of the nucleus-nucleus collision. In a lab-frame collision, the number calculated is simply the average number of collisions one projectile nucleon will experience. In a center of momentum collision between nuclei, the number calculated is the average number of collisions a nucleon inside either nucleus will experience. This average number is Poisson distributed to determine the number of collisions that will occur for each individual nucleon.

- *Picking scattering partners:* Two nucleons are chosen at random from each nuclei and are allowed to scatter when, and if, they meet several criteria. First, the two nucleons cannot have scattered previously. Secondly, the nucleons must be within one cross-sectional radius of one another in the transverse beam direction.

$$\sqrt{(x_t - x_p)^2 + (y_t - y_p)^2} \le \sqrt{\sigma_{NN}/\pi} \tag{4.3}$$

Thirdly, if the collision is proton-induced, the pair must be moving toward one another in the transverse plane. Lastly, the center of mass energy, $\sqrt{s}$, must be above 6 $GeV$. This limit is a parameter within PYTHIA and is chosen to be 6 $GeV$ because it is on the order of the energy where perturbative QCD is no longer applicable and it allows for a decent fit to the lower-energy experimental data considered in this chapter. If the two nucleons meet these criteria, they are allowed to scatter.

- *Scattering and Rescattering:* At this point in the model, PYTHIA determines the nature of the scattering. This entails the determination of the types and kinematics of the initial and final state partons as well as the amount and kinematics of any initial or final state radiation. Using the color connection scheme previously described, strings are formed from partons resulting from the interaction and the diquark remnant of the nucleon. The fragments from the string are determined by JETSET and are stored in a temporary array. Any hadrons that are formed from partonic radiation that is not color-connected to either string goes directly into the nucleus-nucleus final state. The strings that contain the diquark from the original nucleons and therefore the bulk of their energy are then put back into the nuclei and allowed to rescatter as "wounded" nucleons. The wounded nucleon has the string's momentum while its position is updated to halfway between the original nucleons' positions through,

$$(x_1,y_1)(x_2,y_2) \rightarrow \left(\frac{x_1+x_2}{2}, \frac{y_1+y_2}{2}\right). \tag{4.4}$$

This wounded nucleon scenario results in roughly one unit of rapidity lost to the original nucleon each time a scattering occurs. If the wounded nucleon scheme was not used, the simulation not would be able to reproduce the overall number of particles found in the final state because each nucleon-nucleon scattering would have too much energy and would produce too many particles.

- *Final State:* After all nucleons have experienced their geometrically determined number of collisions or the collisions have center of mass energies below the cutoff, particles present in each nucleon's temporary array constitute the final state.

Hadronic observables from the model have been compared against data for several systems. For proton-induced collisions, results from the model were compared against data [34] sets for p+Xe and p+Ar at a lab energy of 200 *GeV*. Figure 4.1, For nucleus-induced collisions, several comparisons to experiment were made. The comparisons between the model and data [35] for O-Au collisions at $E_{LAB}$ = 200 and 60 $GeV$/nucleon are shown in Figure 4.2 and 4.3. Most notable for the work presented in the following chapter, we have made comparisons to S+Au hadronic data. Our model matches the $\pi^0$ spectrum from WA80 [36], as well as the $\pi^-$s from NA35 [37]. The two comparisons are shown in Figures 4.4 and 4.5, respectively. The $p_T$ distribution of neutral pions is slightly above the data at low $p_T$ and slightly below the data for high $p_T$ pions. Although the model is based on very simple premises, it reproduces the main features, rapidity and $p_t$ spectra, characterizing hadronic final states for both proton- and nucleus-induced collisions.

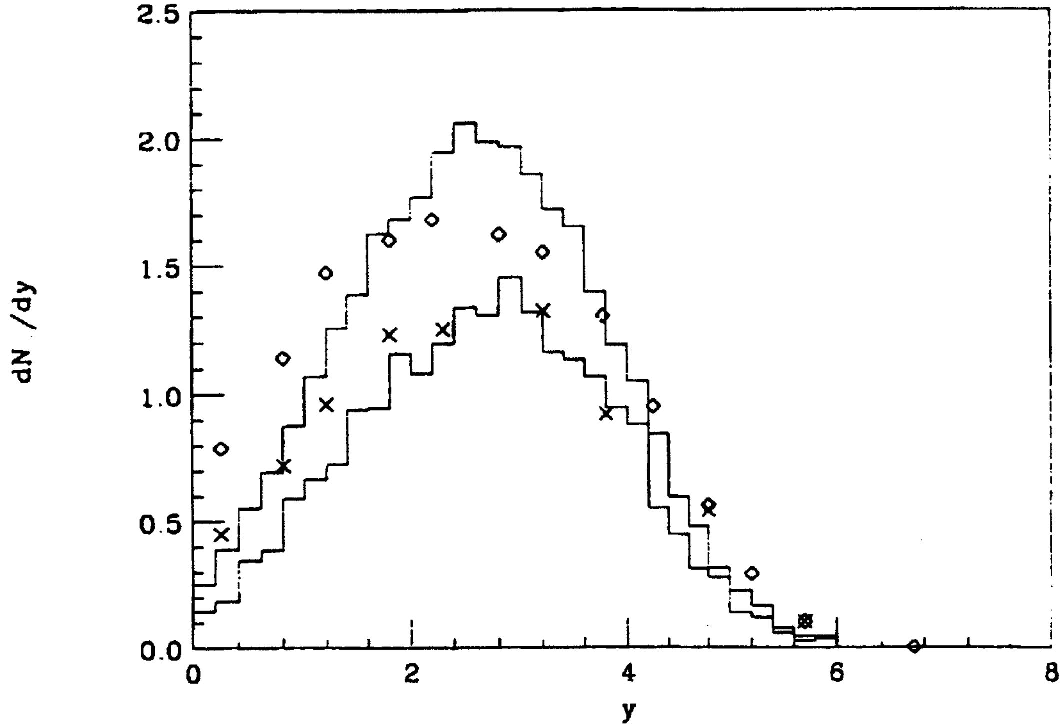

Figure 4.1: Rapidity distributions for p+Ar and p+Xe at $E_{lab} = 200\ GeV/$ nucleon compared with data [34].

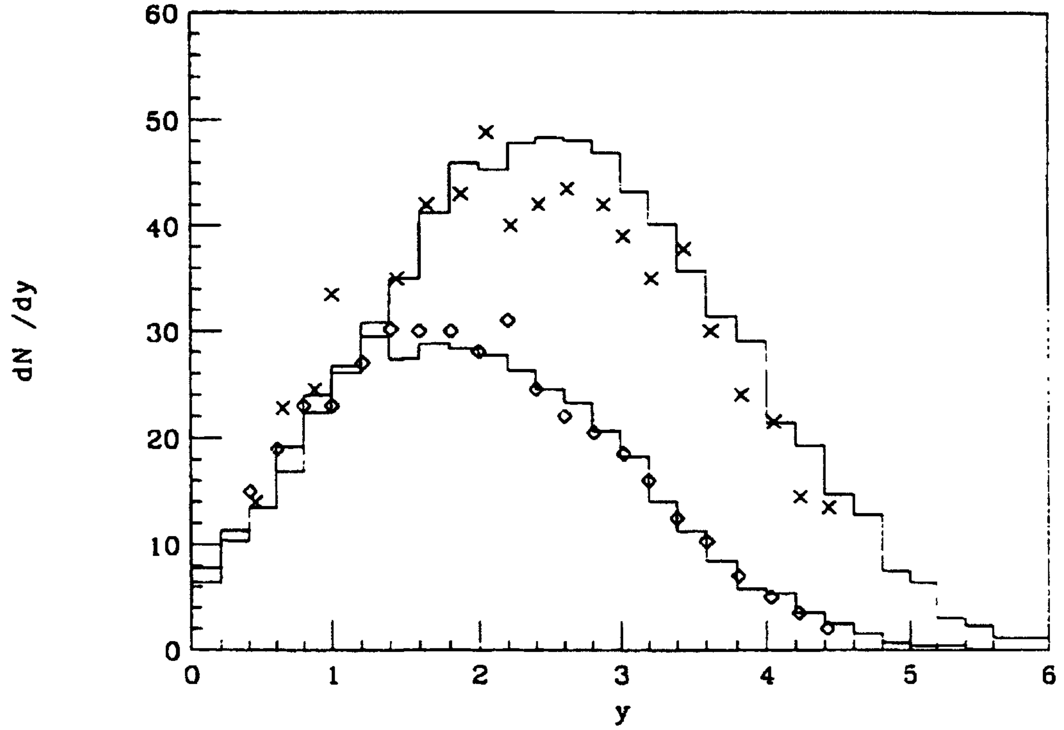

Figure 4.2: Rapidity distribution for O+Au at $E_{lab}$ = 200 and 60 $GeV$/nucleon compared with data [35].

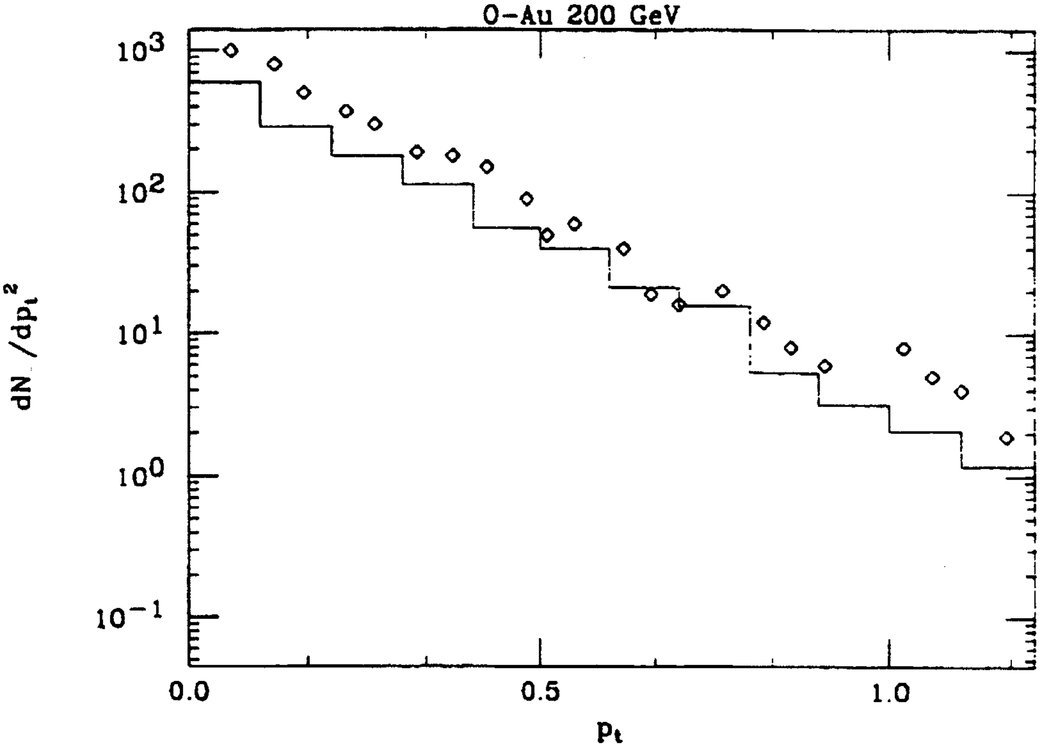

Figure 4.3: $p_t$ distribution for O+Au at $E_{lab} = 200\ GeV$/nucleon compared with data [35].

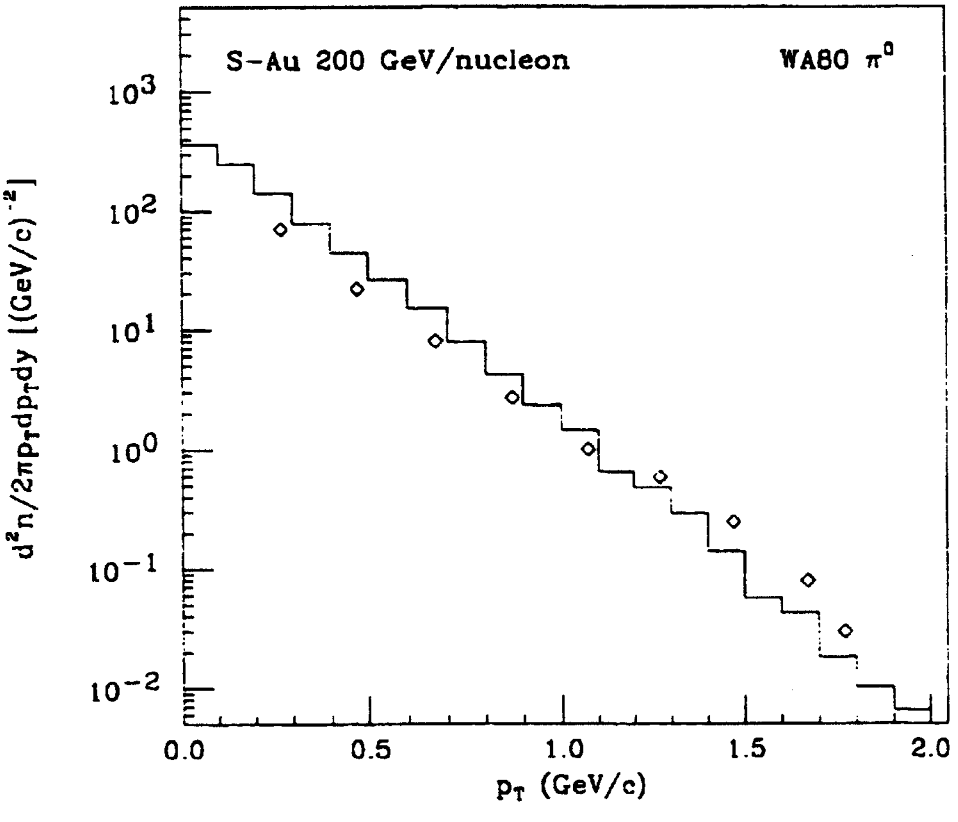

Figure 4.4: $\pi^0$ $p_T$ distribution from WA80 [36] as compared with the model.

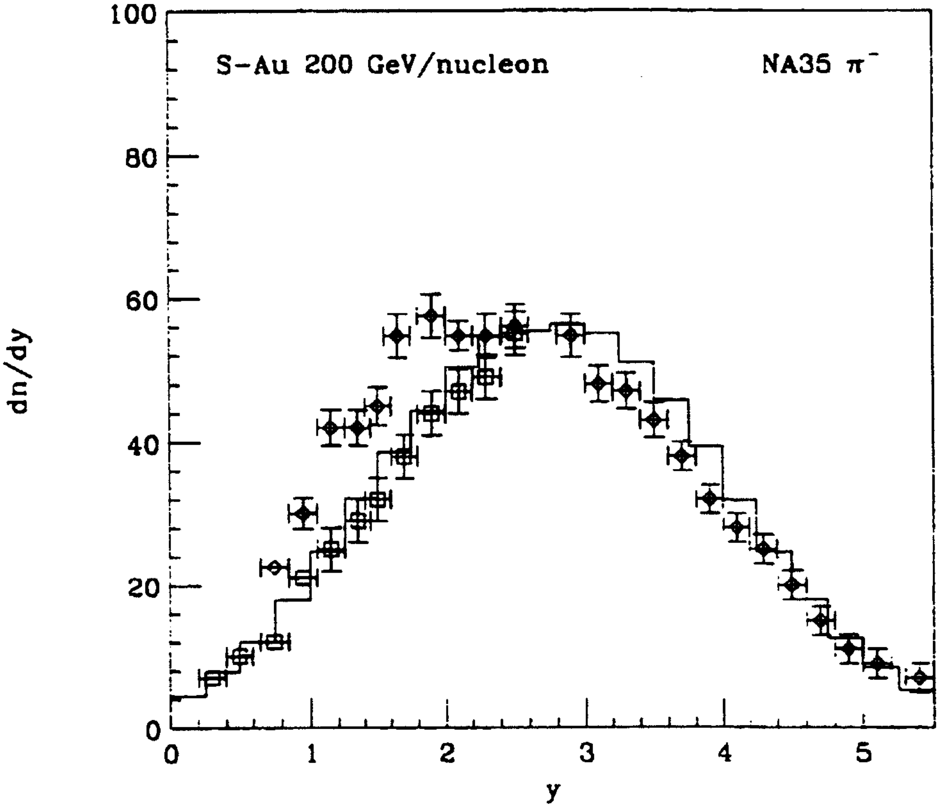

Figure 4.5: $\pi^-$ rapidity distribution from NA35 [37] as compared with the model.

# Chapter 5

# Low-Mass Dileptons from CERN SPS

## 5.1 Introduction

Measuring and analyzing electromagnetic radiation from heavy-ion collisions represents a significant experimental challenge compared to hadronic signals owing to the relatively small cross sections. The additional information they provide certainly justifies the undertaking. Hadrons produced in the initial stages of the collision interact on average several times before leaving the reaction zone. Consequently, any information embedded in hadronic dynamics is completely masked by multiple scatterings. Dileptons are not disturbed by the hadronic environment even though they are produced at all stages of the collisions as they have long mean free paths. They are dubbed "clean probes" of the collision dynamics.

Recent results from the CERES and HELIOS collaborations at CERN [38, 69] have brought about a surge of activity in search of quantitative interpretation. The CERES detector, Figure 5.1, at CERN is dedicated to the study of $e^+e^-$ pairs in relativistic heavy ion collisions. The experiment of particular interest in this chapter studied low invariant mass dileptons from p+Be, p+Au, and S+Au collisions: protons are incident on both targets with a lab energy of 450 $GeV$ and the sulfur projectiles hit the gold targets with a lab energy of 200 $GeV$/nucleon. Only a portion of the lepton pairs can reliably be detected due to acceptance affects. The resulting data is the invariant mass spectrum of lepton pairs with a pseudorapidity between 2.1 and 2.65, an angle greater than 35 *mrad* between leptons, and transverse momenta greater than 50 (100) $MeV/c$ for proton-induced (heavy-ion) collisions.

Predictions were made for the low mass dilepton spectrum based on primary particle production and subsequent radiative and/or Dalitz decays. The proton-induced reactions are consistent with these predictions suggesting that the $e^+e^-$ yields are fairly well understood. Yet, the heavy-ion data (S+Au) show a significant excess as compared to the same model for meson production and electromagnetic decays, Figure 5.2. When integrated over pair invariant mass up to 1.5 $GeV$, the number of electron pairs exceeded the "cocktail" prediction by a factor of 5±2. It is clear that two-pion annihilation contributes in the heavy-ion reactions as fireball-like features emerge and support copious pion production [39]. Vector dominance arguments would naturally lead to extra production around the rho mass. Yet, the excess is most pronounced between the two-pion threshold and the rho mass.

The nature of the enhancement suggests several possibilities [39, 40, 41, 42, 43, 44, 45, 46, 47, 48, 49]. Medium modifications resulting in a shifted rho mass could be responsible [40]. The effects of a dropping rho mass were studied [40] using the relativistic transport model [50]. This model is based on an extended Walecka model for the coupling of light quarks to vector/scalar fields to obtain the form of the medium modified $\rho$ mass. For CERN SPS energies, the initial hadron abundances for the relativistic transport model are taken from RQMD [51]. The inclusion of a dropping $\rho$ mass in the transport model results in a shifted and smeared out mass spectrum for dilepton pairs from $\rho$ decay. Consequently, the mass spectrum predictions from this model fall within experimental data, Figure 5.3.

Along similar lines, consequences arising from a modified pion dispersion relation have been investigated considering finite temperature effects [42] and collisions with nucleons and $\Delta$ resonances [45]. Enhanced $\eta'$ production, as suggested in ref. [46], seems to be ruled out by inclusive photon measurements [52, 53].

Secondary scattering of pions and other resonances has also been studied [54] focusing on the role of the $a_1$ through $\pi\rho \rightarrow a_1 \rightarrow \pi\ e^+e^-$. The contribution was shown to be relevant but not sufficient for interpreting the data.

The study made in this chapter extends the secondary scattering investigation by including non-resonant dilepton-producing $\pi\rho \rightarrow \pi\ e^+e^-$ reactions [55] in addition to the resonant dilepton-producing channels already investigated. In the previous chapter, the event generator providing the basis of the reaction description was detailed. Then in Sec. 5.2 the algorithm used for estimating secondary scattering is introduced and in Sec. 5.3 we discuss normalization and acceptance effects, followed by the results and conclusions in Sec. 5.4.

## 5.2 Secondary Scattering

Dileptons from pseudoscalars ($\pi^0$, $\eta$, $\eta'$) and vectors ($\omega$, $\rho^0$, $\phi$) produced in the primary scattering phase are not enough to account for the S+Au data. Our model also incorporates secondary scattering of hadronic resonances. All pions and rho mesons formed during the primary collisions of nucleons will have a chance to scatter amongst themselves before decaying. The reactions we consider are of two types, one which produces a resonance that decays to dileptons and the other which goes to dileptons directly.

Of the first type, $\pi^+\pi^- \rightarrow \rho^0 \rightarrow e^+e^-$ and $\pi^0\rho^\pm \rightarrow {a_1}^\pm \rightarrow \pi^\pm e^+e^-$ have been included. To accomplish these types of scattering, pions and rhos must of course appear in the final state of the model described in the previous section. As the default, JETSET automatically decays all hadronic resonances, but it also contains provisions to prohibit them. We thus allow neutral pions to scatter from charged rhos when conditions are favorable. Technically, the steps involved in secondary scattering are similar to those for primary scattering.

- *Number of collisions:* The number of collisions is again determined geometrically using the appropriate density and cross section.
- *Picking scattering partners:* A $\pi^+\pi^-$ or $\pi\rho$ pair is randomly chosen and allowed to scatter if (1) the pair has not already scattered, (2) the pair is within one cross-sectional radius of one another in the transverse beam direction. The cross section for creating a $\rho^0$ resonance is taken to be

$$\sigma(\sqrt{s}) = \frac{\pi}{\mathbf{k}^2} \frac{{\Gamma_{\mathrm{partial}}}^2}{(\sqrt{s} - m_{\mathrm{res}})^2 + {\Gamma_{\mathrm{full}}}^2/4} \tag{5.1}$$

with **k** being the center-of-mass momentum. The full and partial decay widths for $\rho^0 \to \pi^+\pi^-$ are set to 152 $MeV$. The situation for creating an $a_1$ resonance through $\pi\rho$ scattering is handled somewhat differently than creating a $\rho^0$ through a $\pi^+\pi^-$ collision. Since our model scatters $\pi$'s and $\rho$'s resonantly and non-resonantly, the cross section used to determine whether or not a pair will scatter should be the total cross section. The total cross section for $\pi\rho$ scattering determines how many and how often the charged rhos scatter with pions. This way the pairs will be chosen according to the total cross section and the normalization of each type of scattering (resonant or non-resonant) will be determined by the branching ratios for each process. This normalization will be explained in greater detail later in the chapter. Since experimental data exists for $\pi\rho$ scattering [56, 57], a parameterization can be used for the total cross section. Based on the general shape of the data. we chose a simple Breit-Wigner shape for the function normalized by what the cross section should be near the $a_1$ peak. The resultant cross section is displayed in Figure 5.4 and parameterized for $\sqrt{s} \geq 0.9\ GeV$ by

$$\sigma(\sqrt{s}) = \frac{0.72}{(\sqrt{s} - 1.1)^2 + \Gamma^2/4)} (mb) \tag{5.2}$$

- *Resonance formation and decay:* The kinematics of the resonances are determined from the pair of hadrons while JETSET decays the resonance into dileptons using appropriate functions for $d\Gamma/dM^2$ and $|\mathcal{M}|^2$ resulting from analysis of a typical Lagrangian [58].

Dileptons from secondary scatterings of the resonance type increase the number significantly in the region around the $\rho^0$ mass. but not in the region with the largest gap. $0.2\ GeV \leq M^2 \leq 0.5\ GeV$.

The non-resonant component is estimated here by computing the sole process $\pi^0\rho^\pm \rightarrow \pi^\pm e^+e^-$. The other $\pi\rho$ channels that contribute to dilepton production involve Feynman graphs that result in a singularity and must be regulated in a full $T$-matrix or some other effective approach [59]. Real photon studies [60. 61. 62] suggest that contributions from $\pi^\pm\rho^0 \rightarrow \pi^\pm e^+e^-$ and $\pi^\mp\rho^\pm \rightarrow \pi^0 e^+e^-$ are comparable to the process we calculated. Therefore we have assumed the same cross section and dilepton mass dependence for the other isospin channels not calculated in this paper. To this level of estimate, isospin averaging and ignoring interference effects between these and the resonant $a_1$ contributions is not worrisome. The prescription for directly scattering pions and rhos is very similar to the one used for resonance scattering as detailed below.

- *Picking scattering partners:* The same prescription used for creating an $a_1$ resonance described previously is also used for picking scattering pairs in non-resonant scattering. The distribution of center of mass energies for the $\pi\rho$ pairs that are allowed to scatter are displayed in Figure 5.5 and are shown to be largely peaked around 1.1 $GeV$. The center of mass energy of a $\pi\rho$ collision has a kinematic lower cut-off, $\sqrt{s}_{min} = m_\pi + m_\rho$. Considering vacuum properties of the $\pi$ and $\rho$, this lower bound on energy should be about 0.91 $GeV$. But Figure 5.5 shows collisions occurring down to about 0.85 $GeV$. This lower cutoff is due to the width of the $\rho$ meson. Since $\Gamma_\rho$ is non-negligible, the $\rho$ mass generated by PYTHIA/JETSET [5] is a Breit-Wigner distribution around the vacuum mass and the simulation might create a $\rho$ with mass less than 0.77 $GeV$ (the vacuum value).

- *Scattering:* Since this is a non-resonant process, the Monte Carlo directly determines the kinematics of the final state. Necessary ingredients for such procedures include an interaction Lagrangian and a resulting squared matrix element. The Lagrangian employed is [60]

$$\mathcal{L} = |D_\mu \Phi|^2 - m_\pi{}^2|\Phi|^2 - \frac{1}{4}|\rho_{\mu\nu}|^2 + \frac{1}{2}m_\rho{}^2|\rho_\mu|^2 - \frac{1}{4}F_{\mu\nu}F^{\mu\nu} \tag{5.3}$$

where $D_\mu = \partial_\mu - ieA_\mu - ig_\rho\rho_\mu$ is the covariant derivative. $\Phi$ is the complex charged pion field, $\rho_{\mu\nu}$ is the rho field-strength tensor and $F_{\mu\nu}$ is the photon field strength tensor. From this Lagrangian, the matrix elements can be determined. In the calculation, the graphs involving the $a_1$ are neglected as the contribution from $a_1$ has already taken into account in the resonance portion of the model. There are three graphs, Figure 5.6, whose matrix elements are listed below.

$$\mathcal{M}_1 = \frac{g_\rho e^2}{M^2(s - m_\pi{}^2)}\epsilon^\mu(p_a)(2p_b + p_a)_\mu(2p_1 + q)_\nu \bar{u}(p_-)\gamma^\nu \bar{v}(p_+) \tag{5.4}$$

$$\mathcal{M}_2 = \frac{h_+(t) g_\rho e^2}{M^2(t - {m_\rho}^2)} \epsilon^\mu(p_a)[{Y_{\mu\nu}}^\alpha](p_b + p_1)_\mu \bar{u}(p_-)\gamma^\nu \bar{v}(p_+) \tag{5.5}$$

$$\mathcal{M}_3 = \frac{g_\rho e^2}{M^2} \epsilon^\mu(p_a)[X_{\mu\nu}]\bar{u}(p_-)\gamma^\nu \bar{v}(p_+) \tag{5.6}$$

where $X_{\mu\nu} = a g_{\mu\nu} + b({p_1}_\mu {p_b}_\nu + {p_b}_\mu {p_1}_\nu) + c({p_b}_\mu {p_b}_\nu + {p_1}_\mu {p_1}_\nu)$

and ${Y_{\mu\nu}}^\alpha = (2p_a - q)_\nu g_{\mu\alpha} - (2p_a - q)_\mu g_{\mu\alpha} - {p_a}_\alpha g_{\mu\nu}$.

In the $t$-channel matrix element, a form factor, $h_+(t) = (\Lambda^2 - m^2)/(\Lambda^2 - t)$, appears to account for the finite size of the mesons. Its presence breaks gauge invariance. In order to completely restore gauge invariance, other terms must be added to the four point diagram $\mathcal{M}_3$: $a = -1$; $b = c = (h_+(t) - 1)/(p_b \cdot q + p_1 \cdot q)$. The parameters $\Lambda$ and $m$ are set to 1.8 $GeV$ and $m_\rho$, respectively.

The absolute square $|\mathcal{M}_1 + \mathcal{M}_2 + \mathcal{M}_3|^2$ and $d\sigma/dM^2$ were used to Monte Carlo the three-body $\pi^\pm e^- e^+$ final state.

The invariant mass distribution, $d\sigma/dM^2$, resulting from the above matrix elements evaluated at $\sqrt{s} = 1.0$ $GeV$ is plotted in Figure 5.7. The dashed curve is the function without form factors present and the solid function has form factors included. The presence of form factors decreases the distribution slightly.

These lepton pairs are of non-resonant origin and are now added to the pairs from resonance decays.

At this point we need to address possible objections to this calculation. In a paper by Li, Ko, and Brown [40], a discussion of other effects which might explain the excess of dileptons is presented. The process in question is $\pi\rho \rightarrow \pi e^+ e^-$. It is stated that the diagrams involved are the same as those needed to calculate the pion polarizabililty in the chiral limit. The work of Holstein [63] is referenced to support the claim that the only contribution to pi rho scattering comes from the $a_1$ channel. The paper by Holstein shows that the diagram responsible for the bulk of the squared matrix element is canceled by a double-rho seagull. leaving only the $a_1$ channel. The calculation done here is actually different from the one referred to by Holstein. The process described there is mediated by a pion whereas the process calculated in this paper has a rho exchange diagram [see Figure 5.6]. Therefore. the processes are not the same. In addition, the Holstein paper calculates the sum of matrix elements for zero momentum transfer. This implies that any cancellation at forward angles is inferred. It is not clear in the paper by Holstein that this cancellation also occurs at non-zero momentum transfer. Furthermore. our calculations are consistent with those by Kapusta et al. [60] for photo-production.

A recent manuscript by Baier et al. [47] attempts a calculation similar to ours. Their results are in contradiction to ours. However. they only used the charged pion and neutral rho reaction. whereas our calculation focussed on the charged rho and neutral pion reaction. In addition. the work by Baier et al. contains kinematic limitations on the dilepton pair that were not made in our study: namely the momentum of the lepton pair was taken to be zero in their estimate. With this in mind and the fact that both calculations look at different processes. it is not clear that the results from Baier. et. al. should be comparable to the results in this chapter.

Another possible problem occurs when comparing our results to photo-production. Several studies have been made into photo-production via the $\pi\rho$ entrance channel. [60. 58. 62]. The work done by Kapusta et al. did not include the diagram $\pi\rho \rightarrow a_1 \rightarrow \pi\gamma$. The other works cited included the $a_1$ resonance in various forms. In the paper by Xiong et al.. the contribution from the $a_1$ resonance channel was comparable if not dominant to the non-resonant calculation by Kapusta, but interference effects between the $a_1$ diagram and the others were not taken into consideration. The study made by Song included these interference effects and showed that the contributions were comparable for one set of Lagrangian parameters and not comparable for a different set. These results seem to contradict the results we find for dilepton production. The relative contributions between the non-resonant and resonant reactions is model dependent, but the sum is not [64, 61]. Therefore, previous real photon studies are not in contradiction with our study of dilepton production.

Since the pions and rhos are scattering inside the reaction zone, their dynamics are altered by the medium. Being of bremsstrahlung type, these mechanisms are therefore susceptible to the Landau-Pomeranchuk-Migdal effect [65]. Pions and rhos involved in secondary scattering will undergo frequent multiple scatterings, and not only with other pions and rhos. Therefore, the number of dileptons produced by this scattering is reduced. The reduction factor is dependent at minimum on the invariant mass of the lepton pair as well as the mean free path of the pions and rhos. We use a reduction $1 - \epsilon^{-M\lambda}$, where $M$ is the invariant mass of the lepton pair and $\lambda$ is the mean free path of the hadrons. For our purposes and level of estimation here, we set $\lambda$ to some average value $\sim 1$ fm [66].

The total dilepton yield from our model is the sum of lepton pairs from primary plus secondary scattering. The invariant mass distributions of the dileptons from all contributions will be discussed in the last section.

## 5.3 Normalization

In order to keep computation time low, the code was run to look at dileptons from $\pi^0$, $\eta$, $\eta'$, $\omega$, $\rho^0$, $\phi$ separately. In each run, the hadron considered was allowed to decay only into the dilepton channel, all other modes were prohibited. Technically, this is merely a way to maximize statistics. To reinstate absolute normalization, all lepton pairs counted were multiplied by the branching ratio for the process from which they came. This approximation is valid because the lepton decay mode is a comparatively rare event. We have successfully used this perturbative technique before to calculate high-energy photon production in the framework of BUU transport theory [67]. The secondary scattering resonance production was handled much the same way. All resonances produced from secondary scattering decayed exclusively into their lepton channels and were later multiplied by the appropriate branching ratio. Normalization procedures for non-resonance $\pi\rho$ scattering is somewhat different. Instead of a branching ratio from the particle data book as before [68]. the fraction of $\pi\rho$ events that result in lepton pairs in the final state is based on the calculated cross section for $\pi\rho \rightarrow \pi e^+e^-$ divided by the total cross section for $\pi\rho$ scattering. As a test as to whether or not the total cross section used is reasonable. we looked at the fraction of $\pi\rho$ events that result in real photon production using the same total cross section for $\pi\rho$ scattering. This fraction is comparable to the branching ratio for $a_1 \rightarrow \pi\gamma$ and therefore consistent with results from other papers studying the relative contributions from the two channels [58. 62].

The experimental data our simulation is compared against has several kinematic cuts made on it. To keep our results consistent with experiment. the acceptance for the data was also used on the results from the model. An example of the affect of kinematic cuts on our model's results is seen in Figure 5.8 for cuts made on dileptons from $\pi\rho$ scattering

## 5.4 Results

The invariant mass spectra of dileptons from the primary scattering part of our model for three different systems are displayed in Figures 5.9. 5.10. and 5.11. The first two plots display lepton pairs from p+Be collisions and p+Au collisions, respectively. Figure 5.11 shows dileptons in question from S+Au collisions. The simulation agrees with the proton-induced data and it is reassuring that our S+Au model-results are consistent with the cocktail from the CERES collaboration [38]. Plotting against the actual S+Au data reveals a significant enhancement over predictions in the invariant mass region between 200 and 500 $MeV$. There is also a modest enhancement for masses above this range.

Dileptons from secondary scattering for the S+Au system in our model are shown in Figure 5.12. The contribution from pion annihilation increases the distribution significantly in the rho mass region, but still leaves an excess below the rho mass. We should stress that we have taken vacuum rho properties throughout. Radiative $a_1$ decay contributes a minimal amount in the excess (or deficit) region, but the contribution from non-resonance $\pi\rho$ scattering provides the largest increase in the region of excess.

With the inclusion of the secondary scattering previously described, the invariant mass distributions of dileptons are shown in Figures 5.13, 5.14, and 5.15. The dilepton spectra from the proton-induced interactions, Figures 5.13 and 5.14, are not significantly changed. This result is as expected—dileptons from the smaller systems are quantitatively described by primary hadronic decays. The proton-nucleus collisions do not create a heated nuclear medium large enough or dense enough to bring about significant collective effects. Conversely, the S+Au collision has a non-negligible increase in lepton-pair production between an invariant mass of 200 and 500 $MeV$ as well as a noticeable increase in the higher mass region, Figure 5.15. It is not surprising that secondary scattering becomes important in the S+Au system, as a dense nuclear medium is created during the collision.

The same mechanisms used to study the dielectron excess present in the CERES data can also be used to investigate the excess of muons in the HELIOS/3 data [69]. These calculations were performed. and similar results were seen. Figures 5.16 and 5.17. The p+W interaction is well predicted by decaying mesons ($\eta$. $\omega$. $\eta'$. $\rho^0$. $\omega$. $o$) and the S+W collision reports a small excess over these decays. When the secondary scattering described in this paper is included. both sets of experimental data are somewhat matched by the results of the simulation.

Allowing for the short-comings of our model. results still suggest that secondary scattering is an important but not complete explanation of the excess found in dilepton data. Further studies suggest [70] that even though rescattering is not a strong contributor to the overall dilepton yield in the low mass region. its presence is significant in the collisional broadening of the in-medium rho meson mass. Inclusion of secondary scattering, 1) preserves the consistency the primary scattering in our model has with proton-induced data and. 2) enhances the number of dileptons within the region of excess discovered in S+Au data. Although the contributions from $\pi\rho$ scattering cannot rule out other possible explanations for the excess electrons. the simplicity of rescattering is attractive.

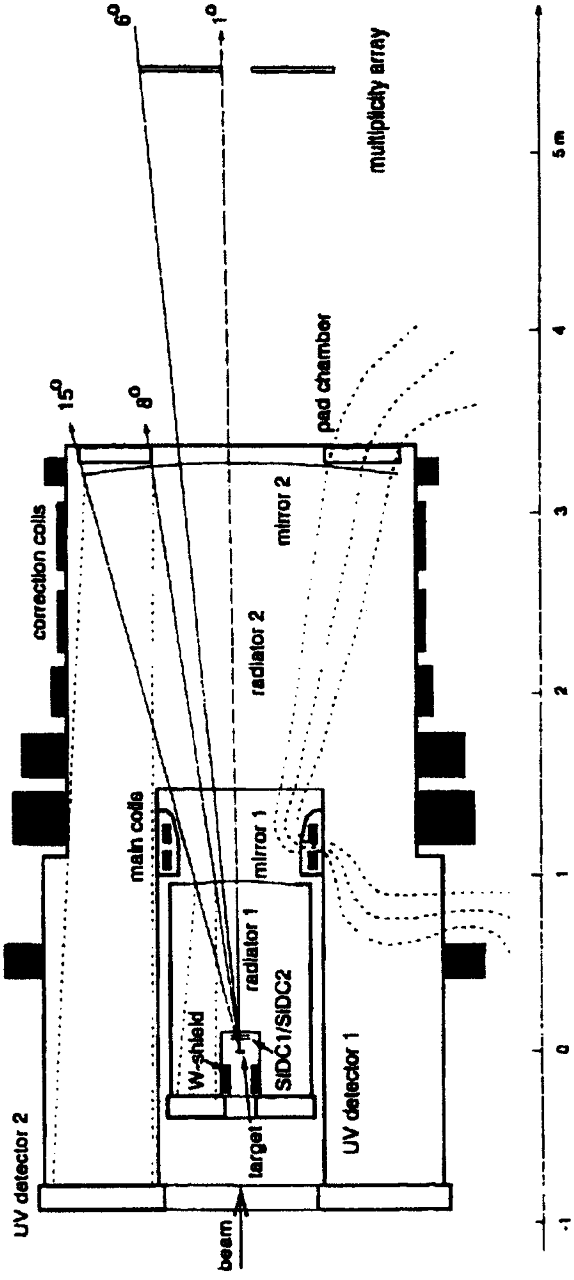

Figure 5.1: Schematic diagram of CERES detector [38].

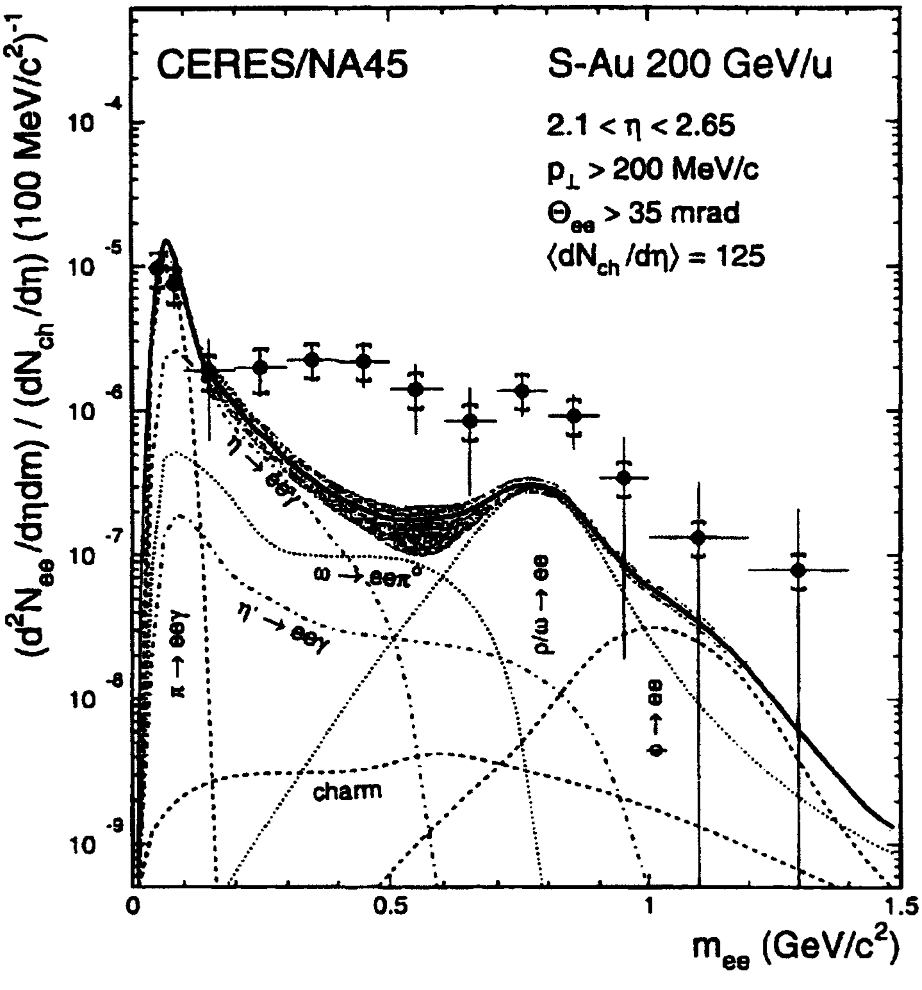

Figure 5.2: Predictions and data for S+Au at 200 $GeV$/nucleon from CERES collaboration [38].

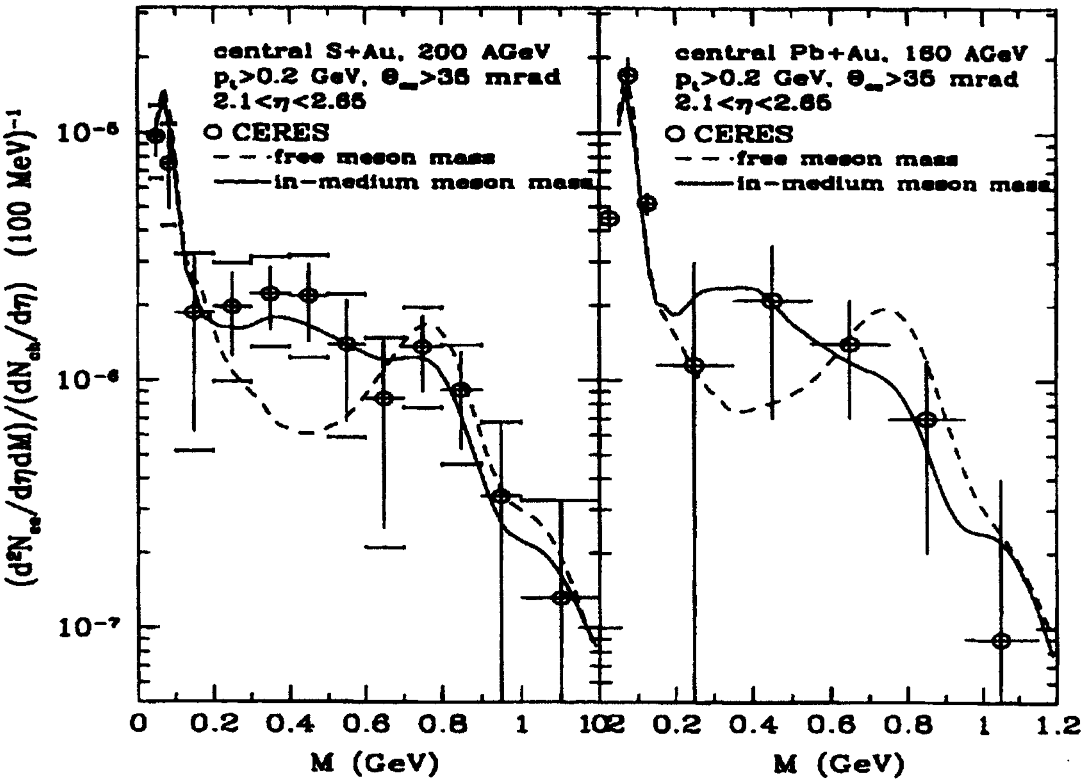

Figure 5.3: Dilepton invariant mass spectra, including contributions from an in-medium shift in the $\rho$ mass, compared to CERES data [40].

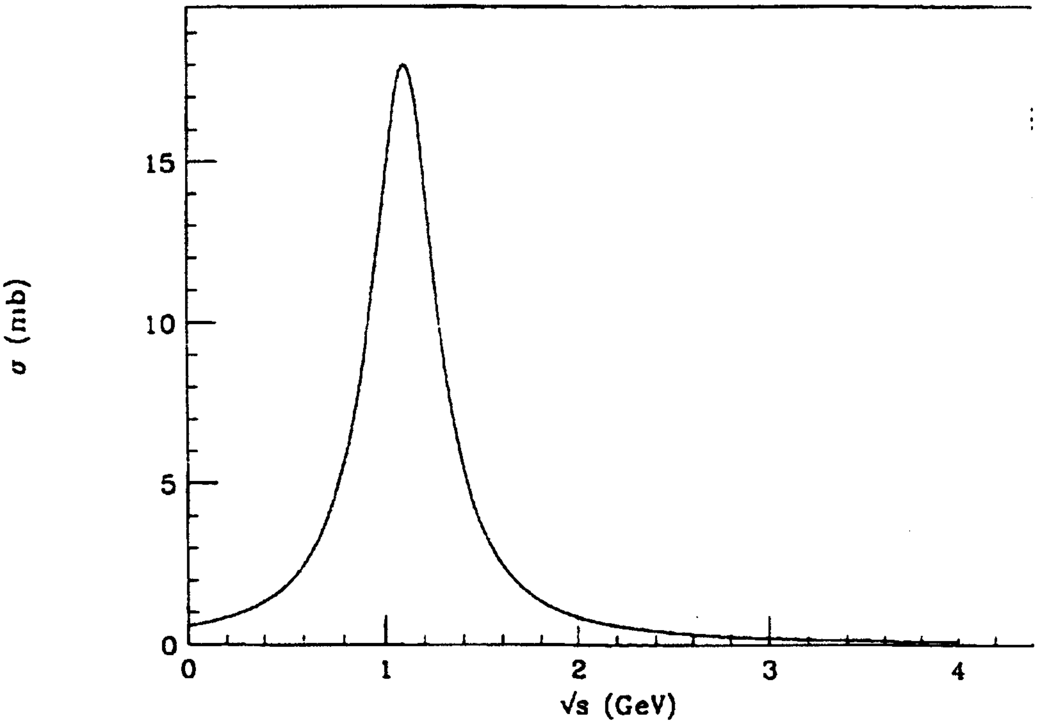

Figure 5.4: Total cross section used for $\pi\rho$ scattering parameterized from data [43, 44].

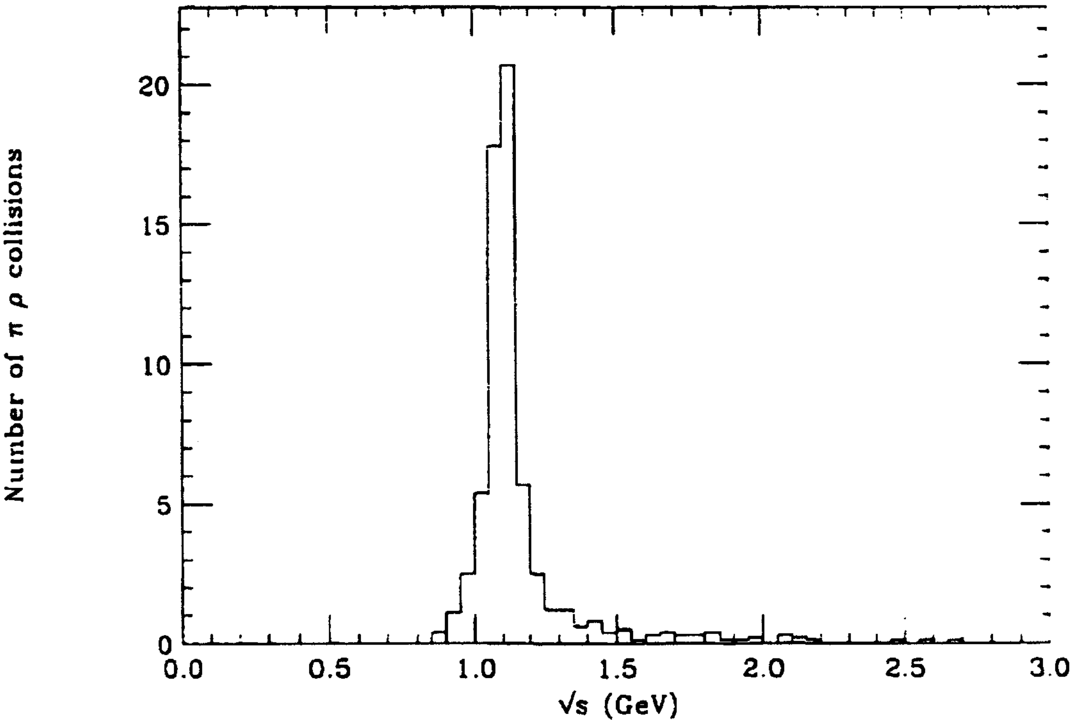

Figure 5.5: Distribution of center of mass energies for $\pi\rho$ scattering in a S+Au collision at $E_{LAB} = 200\ GeV$/nucleon.

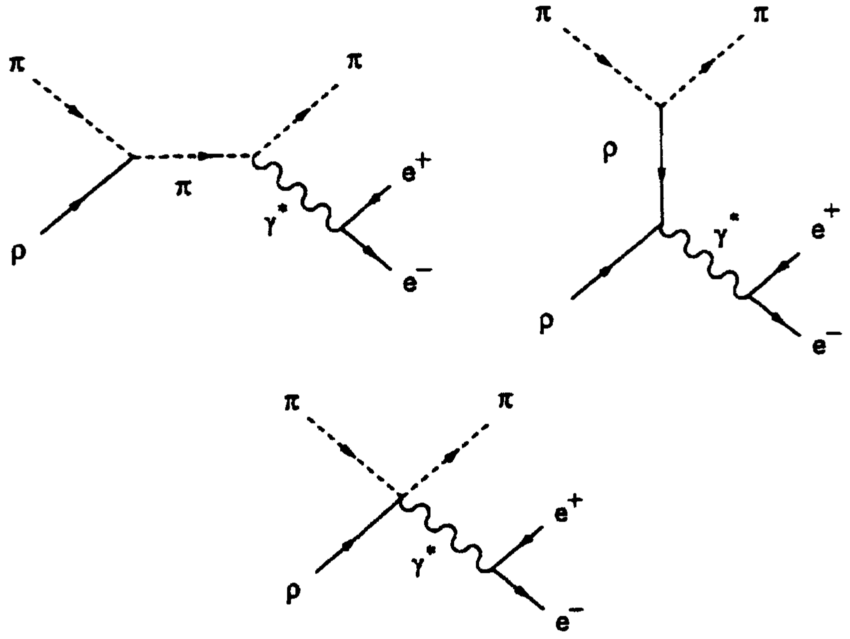

Figure 5.6: Contributing Feynman diagrams for $\pi\rho \rightarrow \pi e^+e^-$.

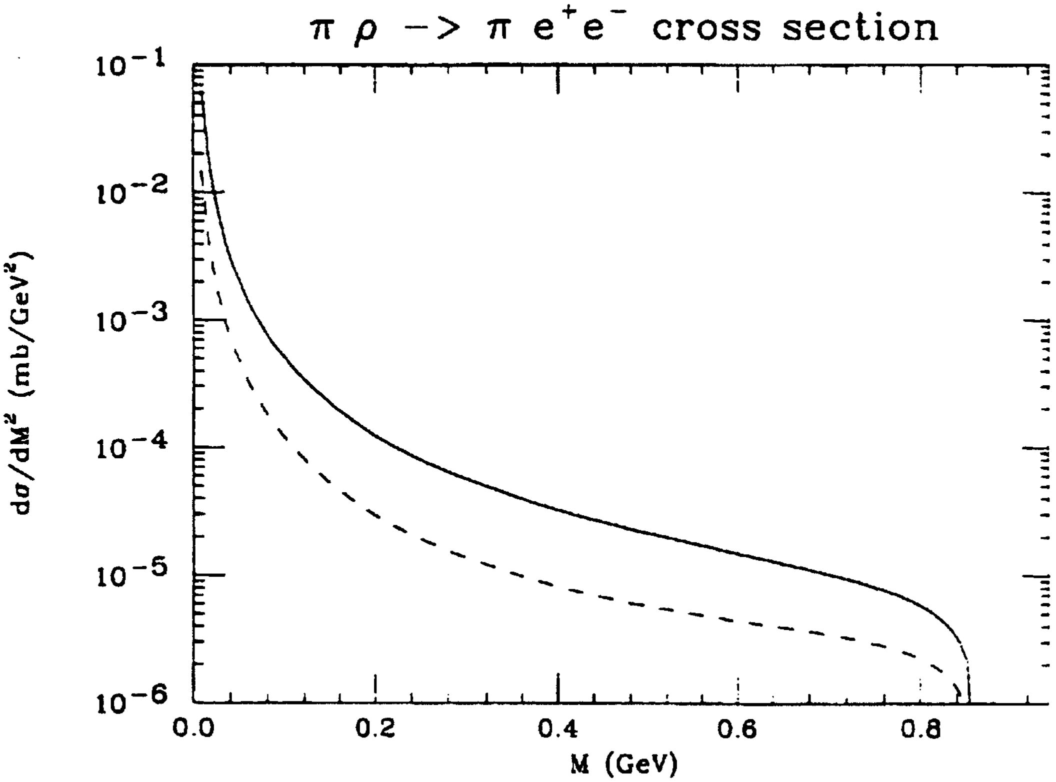

Figure 5.7: Invariant mass distribution of cross section for $\pi\rho \rightarrow \pi e^+e^-$ with the solid curve as the calculation without form factors and the dashed curve as the calculation including form factors.

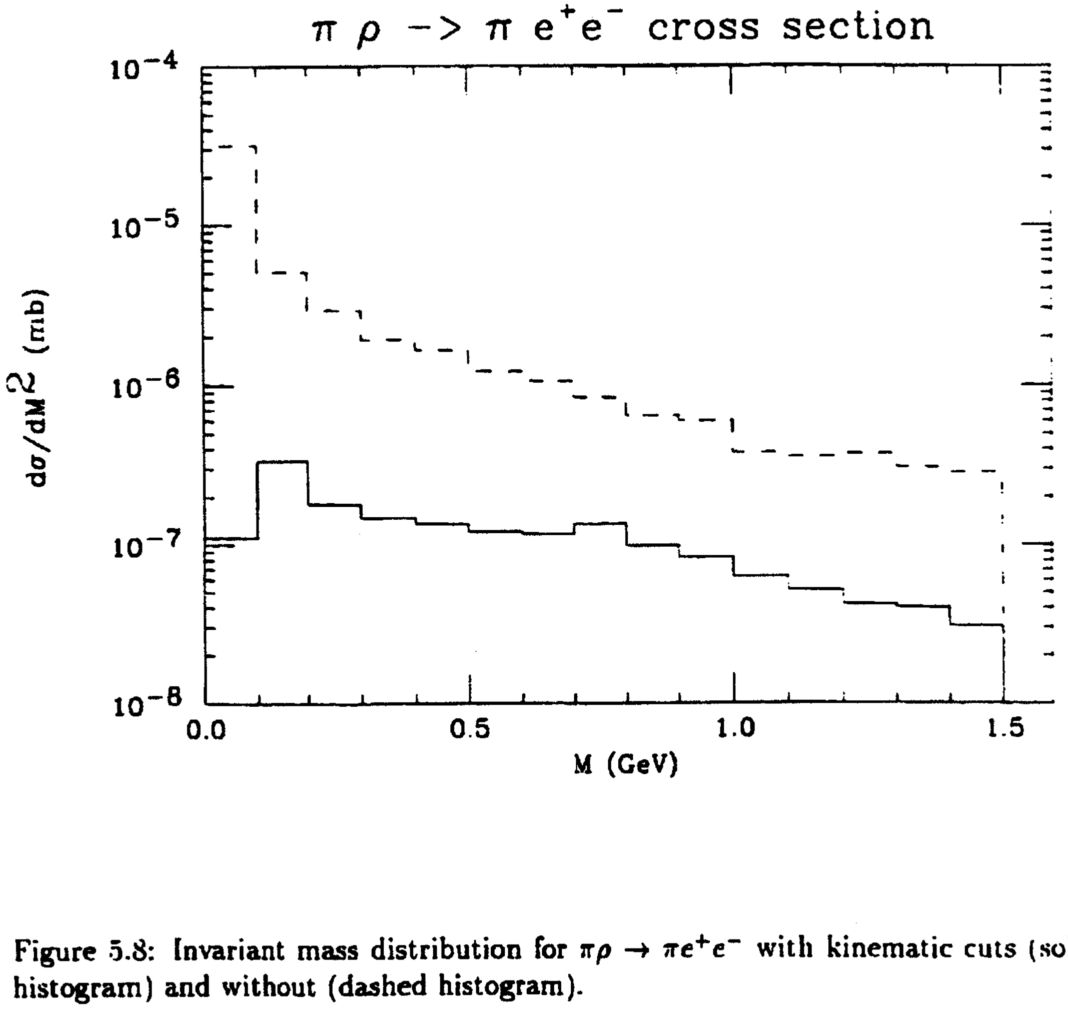

Figure 5.8: Invariant mass distribution for $\pi\rho \rightarrow \pi e^+e^-$ with kinematic cuts (solid histogram) and without (dashed histogram).

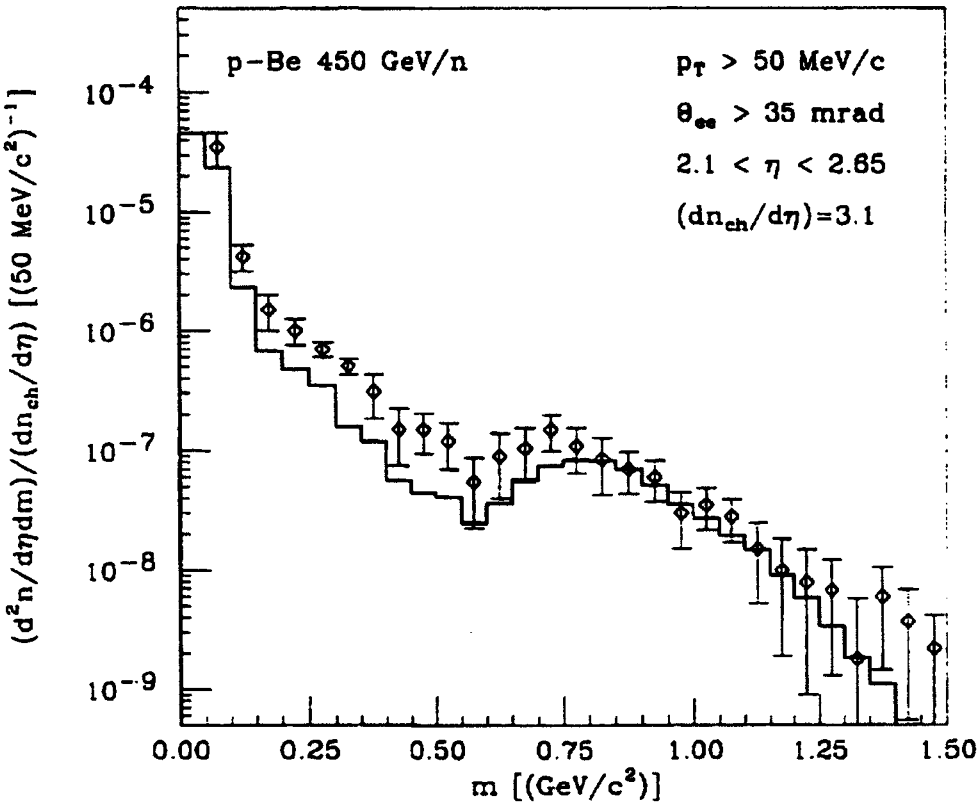

Figure 5.9: Dilepton invariant mass spectra from primary scattering in the model compared to CERES data [38] for p+Be collisions at $E_{lab} = 450$ *GeV*.

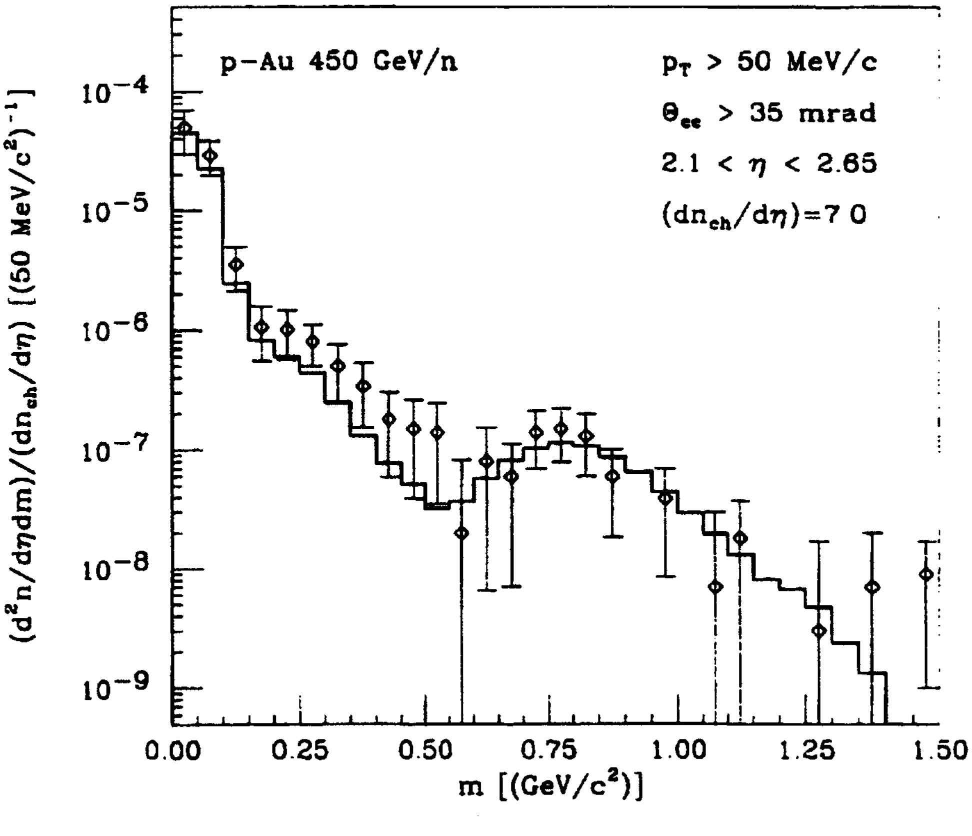

Figure 5.10: Dilepton invariant mass spectra from primary scattering in the model compared to CERES data [38] for p+Au collisions at $E_{lab} = 450\ GeV$.

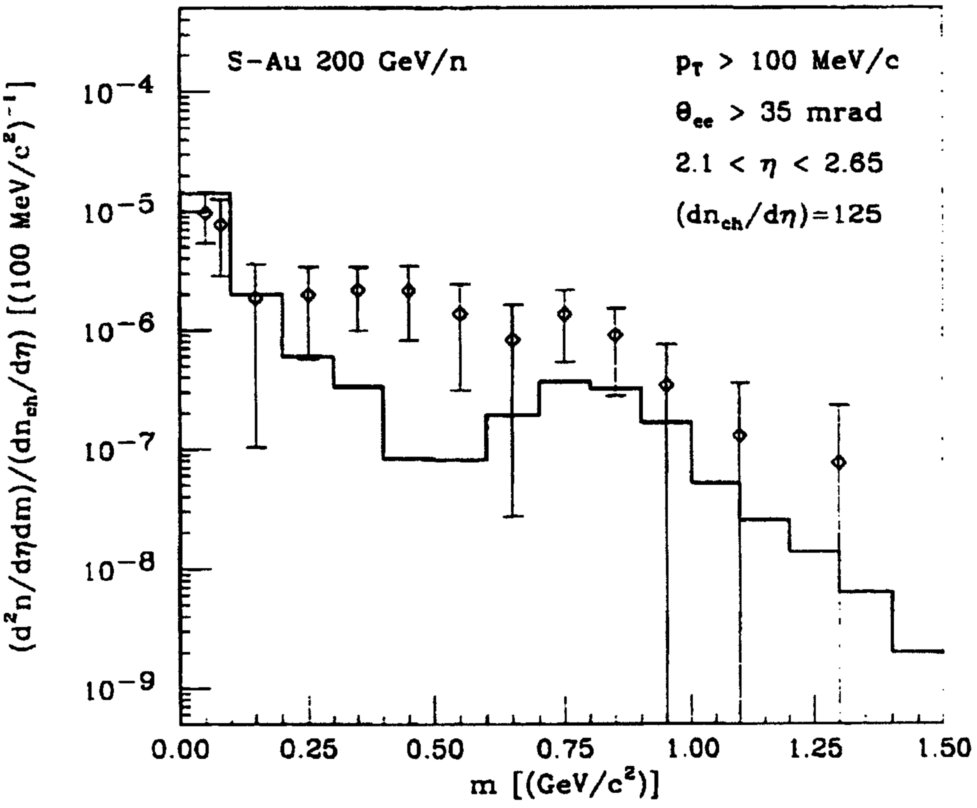

Figure 5.11: Dilepton invariant mass spectra from primary scattering in the model compared to CERES data [38] for S+Au collisions at $E_{lab} = 200$ $GeV$.

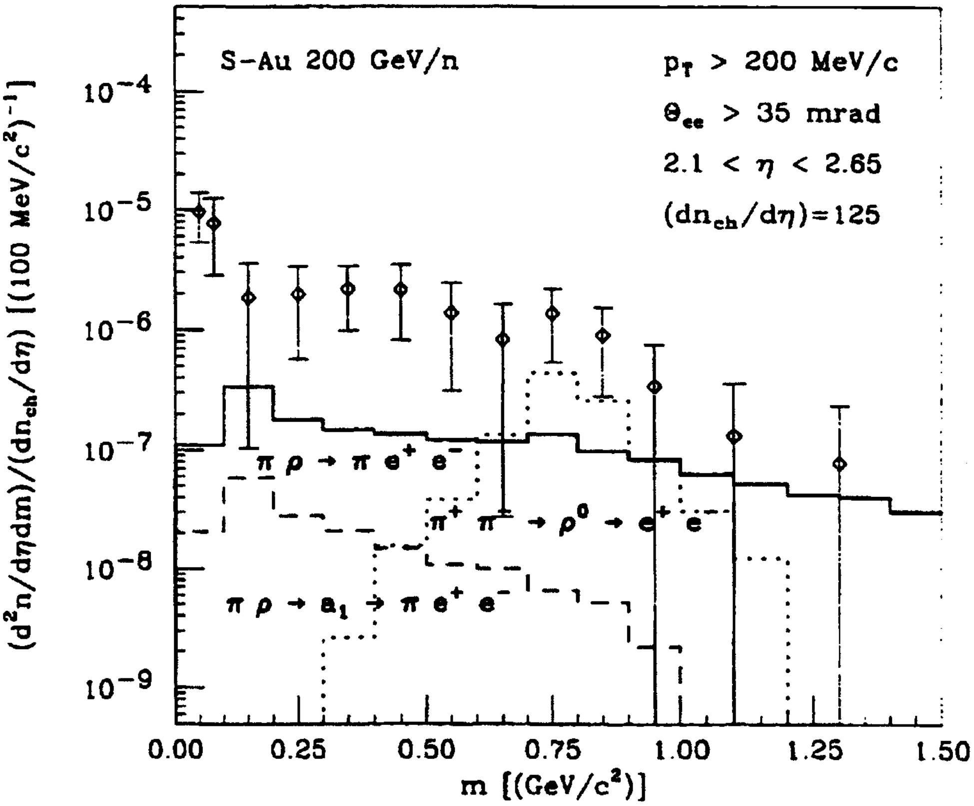

Figure 5.12: Contributions from secondary scattering in S+Au collision.

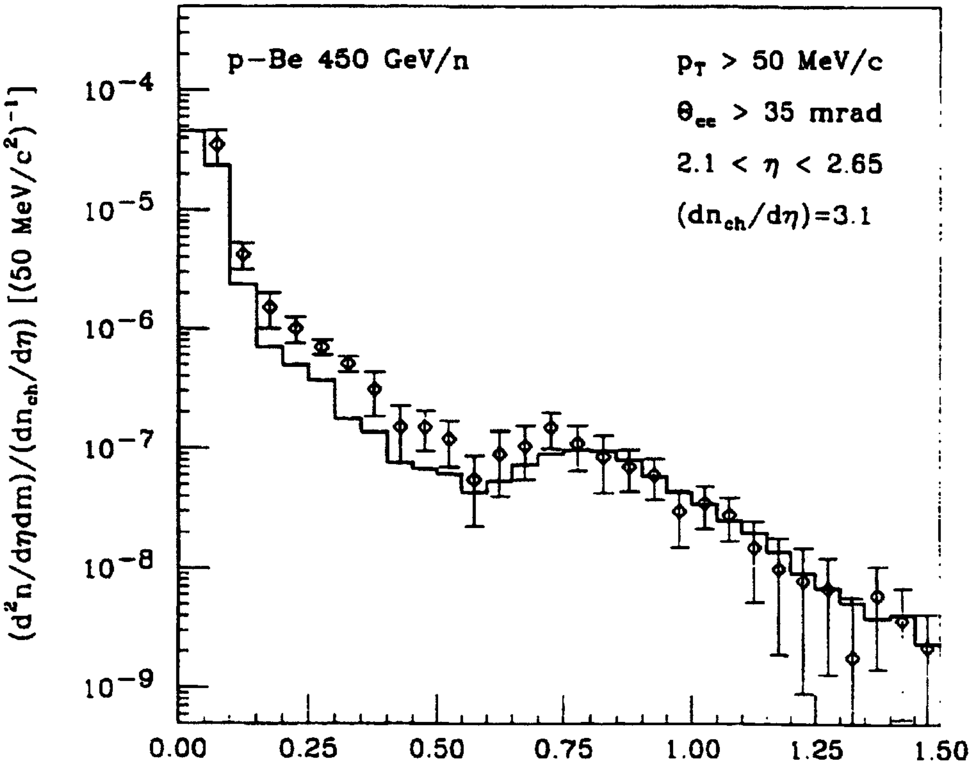

Figure 5.13: Total dilepton invariant mass distributions, including primary and secondary scattering in the model as compared with CERES p+Be data [38].

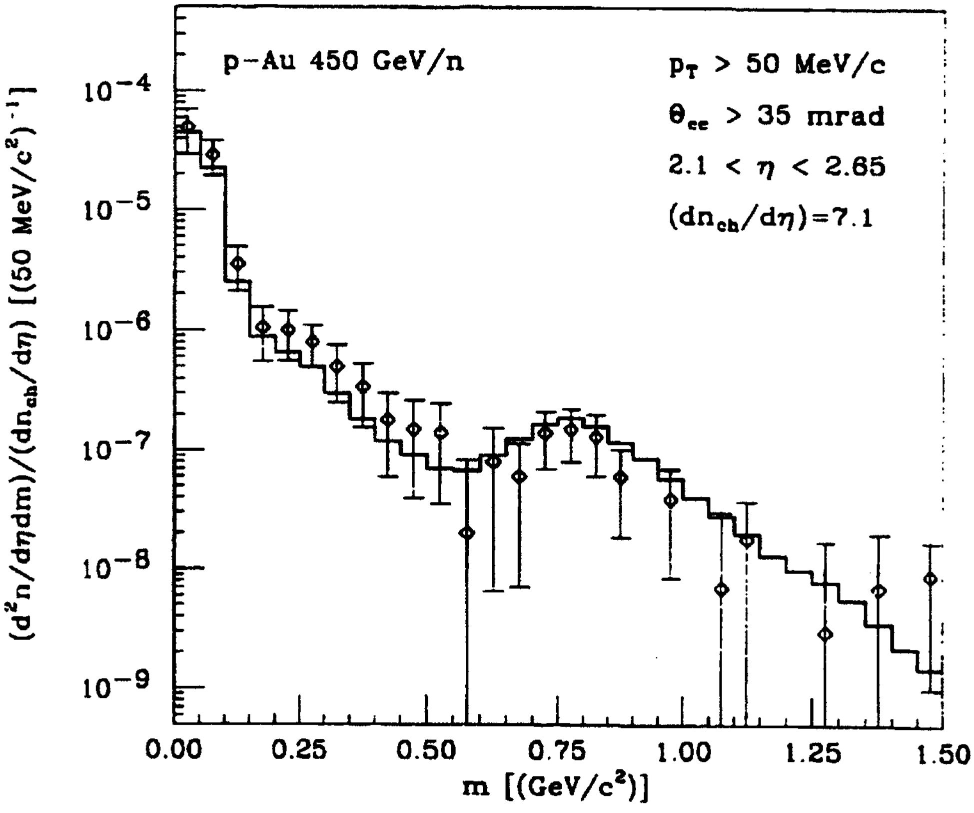

Figure 5.14: Total dilepton invariant mass distributions, including primary and secondary scattering in the model as compared with CERES p+Au data [38].

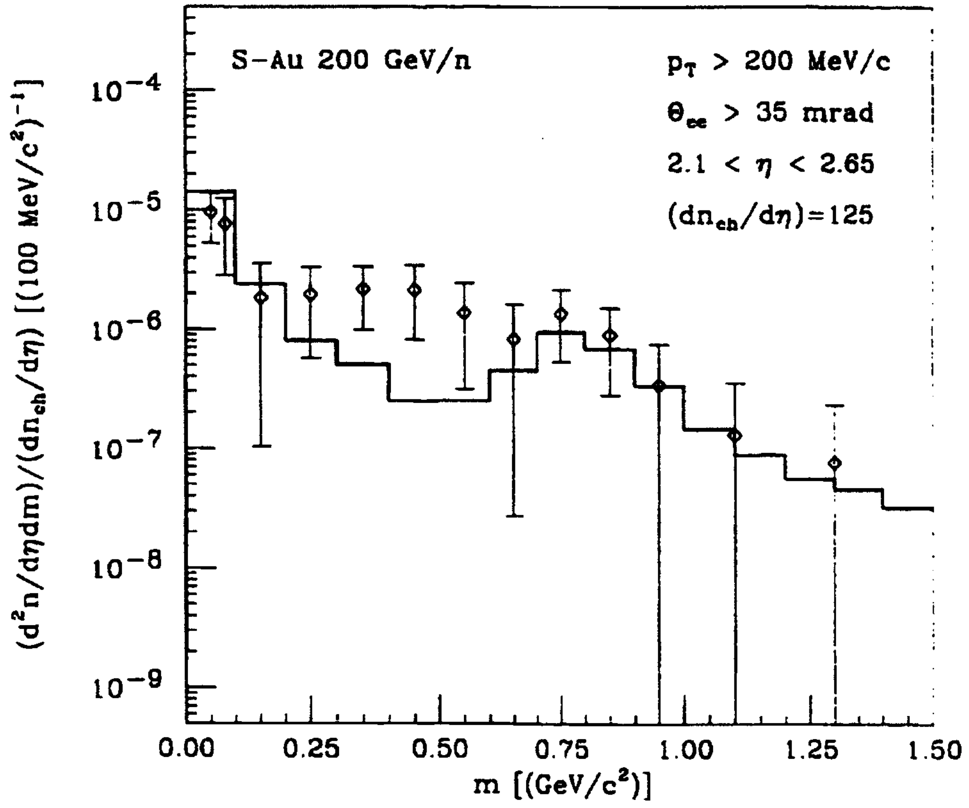

Figure 5.15: Total dilepton invariant mass distributions, including primary and secondary scattering in the model as compared with CERES S+Au data [38].

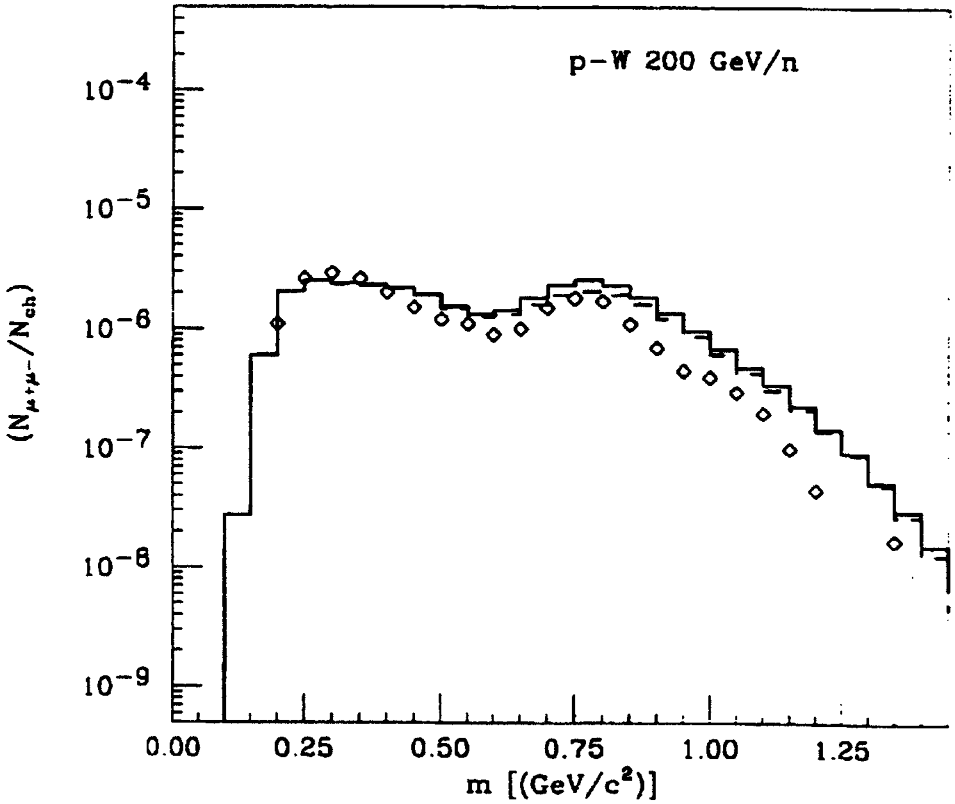

Figure 5.16: Total dimuon invariant mass distributions, including primary and secondary scattering in the model as compared with HELIOS p+W data [69].

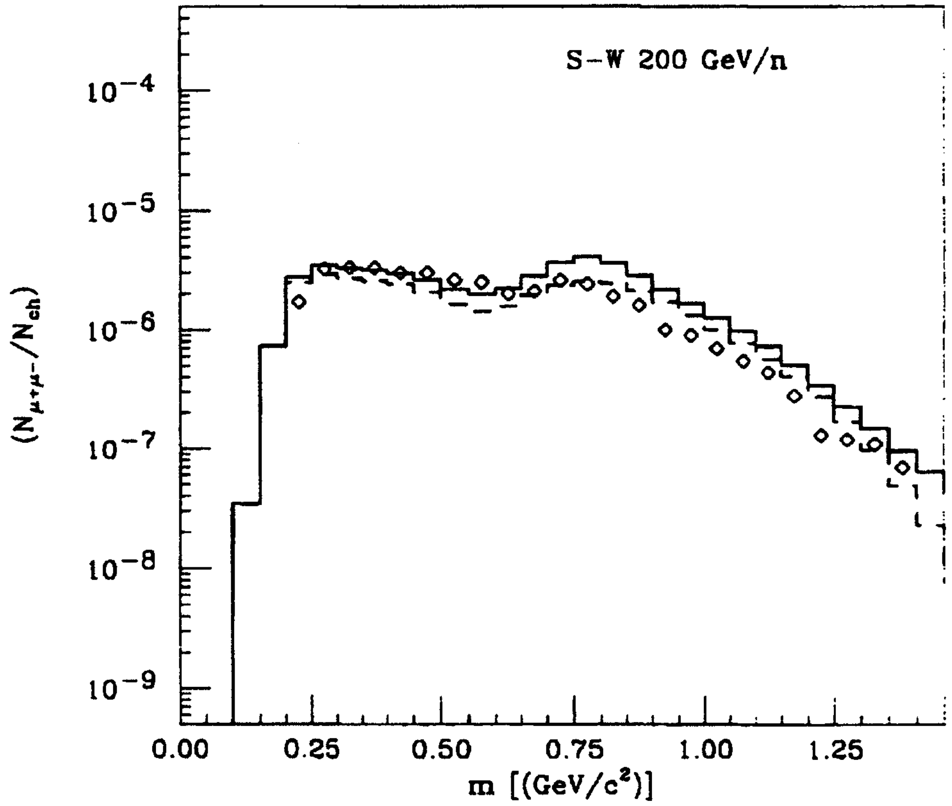

Figure 5.17: Total dimuon invariant mass distributions, including primary and secondary scattering in the model as compared with HELIOS S+W data [69].

# Chapter 6

# Secondary Scattering in a RHIC Simulation

## 6.1 Introduction

In low-energy heavy ion collisions, the produced particles free-stream toward the detector and rarely interact among one another. As heavy-ion collisions energies increase, the interactions between produced particles become more frequent. Therefore, one would expect that these secondary collisions become more important. In a Au-Au collision at $\sqrt{s} = 200\ GeV$/nucleon, the hadrons produced by string fragmentation are still energetic enough to collide with other hadrons produced at the same stage of the collision. Since these scatterings are typically above the perturbative QCD cutoff, it is necessary to characterize the collisions with perturbative QCD. The details of secondary scattering are similar to primary scattering and are outlined in the next section.

The study presented in this chapter focuses on the effects of secondary scattering in nucleus-nucleus collisions: an effect not present within HIJING [4]. This study will show that, as time before freeze-out increase, collisions between produced hadrons play a significant role in the dynamics and observables of the nucleus-nucleus collision.

## 6.2 Secondary Scattering

Secondary scattering in our model is achieved by turning off all particle decays within JETSET. This results in an intermediate state consisting of various undecayed particles. These intermediate state particles are allowed to scatter in a manner similar to the initial nucleon collisions, via the parton model and pQCD. Collisions between produced particles continue until the geometrically determined number of collisions is reached. After which, all unstable particles produced are allowed to decay and the final state is formed.

Ideally, all of the particles in the intermediate state would be allowed to scatter. At present, PYTHIA includes provisions to simulate scattering of a small number of these particles. In addition to neutrons, protons, and their anti-particles, collisions with different species of $\pi$, $\Sigma$, $\Lambda$, $\Xi$, $\Omega$, and their anti-particles can be simulated. This restricted number of particle types PYTHIA can model scattering for is due to the lack of available parton distribution functions for all types of hadrons. Some distributions are available for particles other than the proton and neutron. PYTHIA includes pion parton distribution functions determined by Duke and Owens [71]. Unfortunately, less than 50% of the intermediate state described consists of particles types recognized by PYTHIA as possible initial state particles. To account for a larger percentage, all possible $\rho$ charge states were included by assuming the same parton distribution for $\rho$ as for $\pi$. In the future, this assumption could be extended to include many other particles. Kaons and other mesons should have parton distributions similar to pions and deltas or other higher mass hadrons should assume parton structure similar the the proton or neutron.

## 6.3 Nuclear Shadowing

An important consideration that must be made in simulation of heavy-ion collisions at high energies is the effect of nuclear shadowing. The nuclei. in a high energy heavy-ion collision. are highly Lorentz-contracted; creating a nucleus densely populated with partons. One would expect that interactions between partons inside the same nucleus might become important. Indeed. there is experimental evidence that the number of low-momentum fraction quarks in a nucleus is reduced over the number expected from simple addition of nucleon distributions [72]. There are a number of proposed explanations for this reduction in low-x partons [73. 74. 75. 76. 31]. These explanations attribute nuclear shadowing to gluon recombination at high densities. At present. data exist to constrain the amount of quark shadowing in these models. but not the amount of gluon shadowing. In the simulation described within this thesis. quark and gluon shadowing are assumed to be similar and are implemented in the same fashion that shadowing was implemented inside HIJING [4]. The following parameterization is consistent with the nuclear dependence proposed in references [74. 76].

$$\begin{aligned} R_A(x) = 1 + 1.19 ln^{1/6}[A(x^3 - 1.5(x_0 + x_L)x^2 + 3x_0 x_L x)] \\ -[\alpha_A - \frac{1.08(A^{1/3} - 1)}{ln(A+1)}\sqrt{x}]e^{-x^2/x_0^2} \end{aligned} \tag{6.1}$$

where $R_A(x) \equiv (f_{a/A}(x))/(Af_{a/N}(x))$. When shadowing is included. the overall multiplicity is naturally reduced. Figure 6.1 displays this depletion compared to the depletion within HIJING when shadowing is included (symbols). The charged particle multiplicity is reduced by a factor that is consistent with HIJING's findings on nuclear shadowing.

## 6.4 Results

A model that includes scatterings between produced particles should also be able to reproduce lower energy data where secondary collisions are not expected to be important. With this in mind, the simulation was run for O-Au at $E_{lab} = 200\ GeV$/nucleon ($\sqrt{s} \simeq 19\ GeV$/nucleon) and compared to existing data [35] for negatively charged particle rapidity distributions, Figure 6.2. Secondary scattering, as expected, does not contribute significantly to the particle multiplicity. When the simulation is run for Au-Au collisions at $\sqrt{s} = 200\ GeV$/nucleon, the results are quite different. The pseudorapidity distributions of charged particles from our model compared to HIJING calculations [4] and the $p_t$ distribution of negatively charged particles is shown in Figure 6.3 and Figure 6.4. In the collision of higher mass ions, the particle multiplicity that originates from secondary scattering is significant and increases the overall multiplicity by roughly 50% but the $p_t$ distribution is not significantly changed.

The results of our model including shadowing and secondary scattering are compared to prediction from HIJING [4] in Figure 6.5. The data points, from HIJING predictions, contain treatments for nuclear shadowing as well. When secondary scattering is included, this model exceeds HIJING's multiplicity prediction, but is still below predictions from parton cascade models [2]. The total multiplicity is an important factor in the design of detectors at RHIC. This implies that inclusion of secondary scattering is an effect that must be studied further in order to simply understand the particle multiplicity of Au+Au collisions at RHIC.

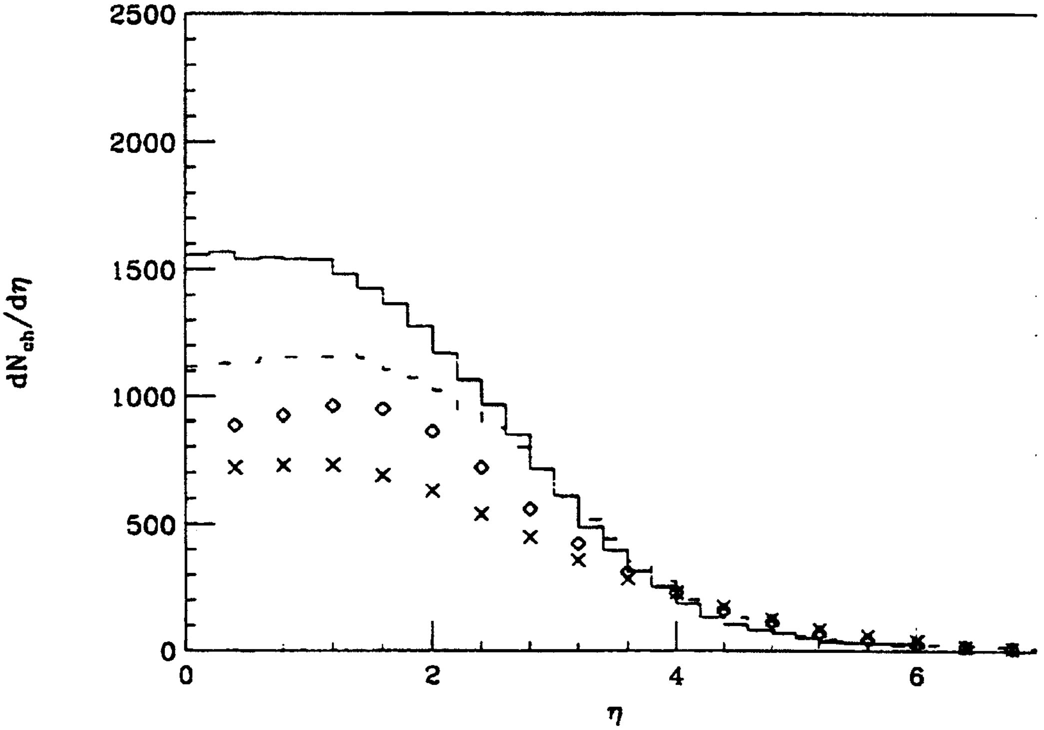

Figure 6.1: Charged particle pseudorapidity distribution for Au+Au with (solid histogram) and without (dashed histogram) nuclear shadowing compared to HIJING data [4] with (cross data points) and without (diamond data points) nuclear shadowing.

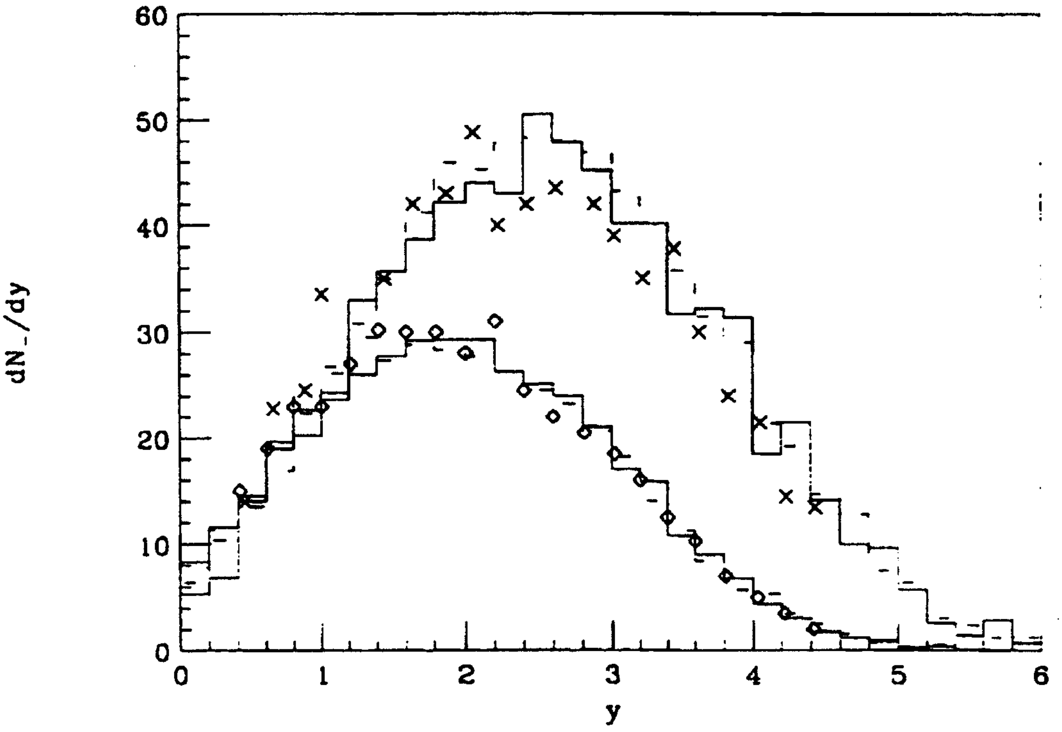

Figure 6.2: Negatively charged particle rapidity distribution for O+Au at $E_{LAB}$ = 200 and 60 $GeV$/nucleon including secondary scattering compared to data [35].

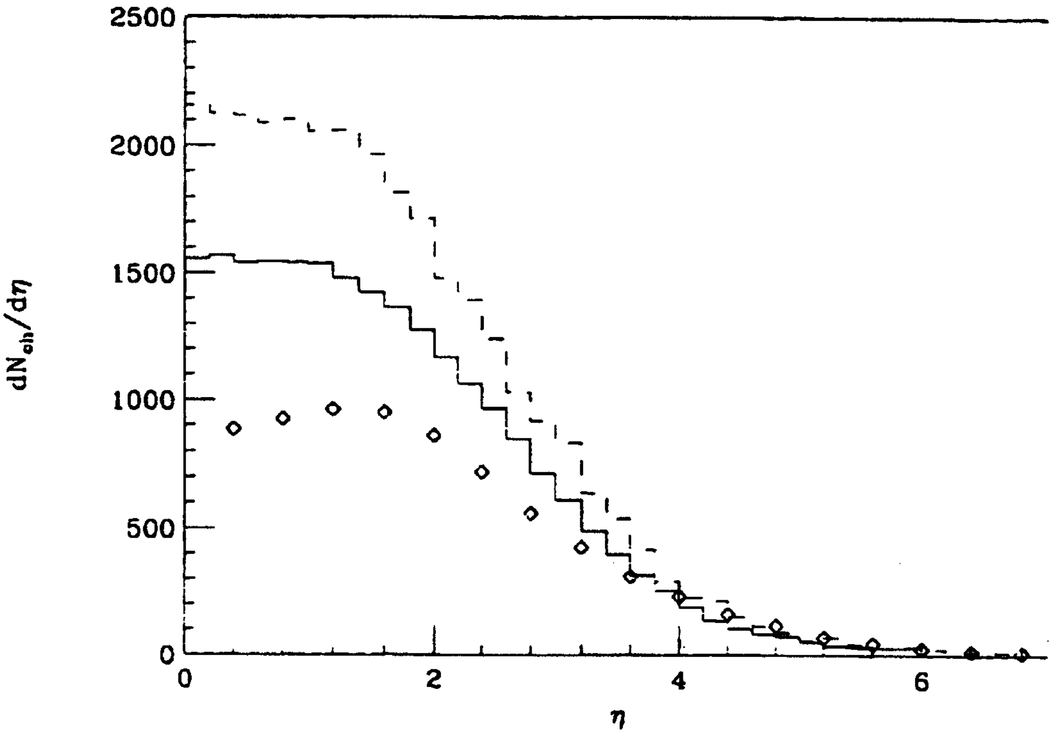

Figure 6.3: Charged particle pseudorapidity distribution for Au+Au with (solid histogram) and without (dashed histogram) secondary scattering compared to HIJING calculation [4] (symbols).

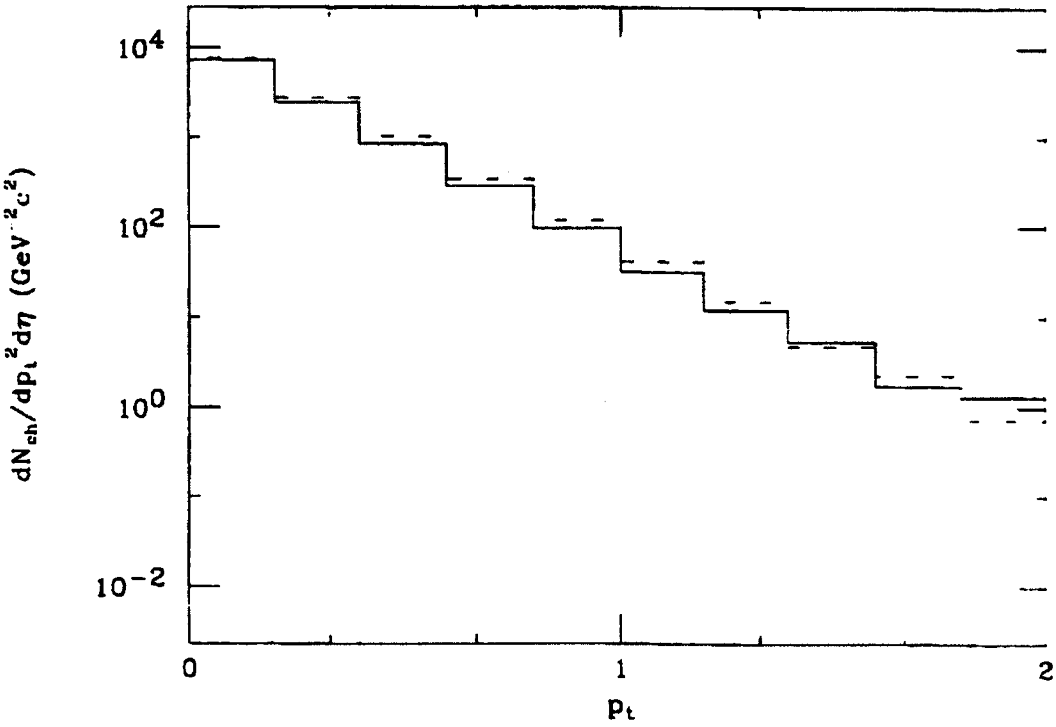

Figure 6.4: Charged particle $p_t$ distribution for Au+Au with shadowing and secondary scattering (solid histogram).

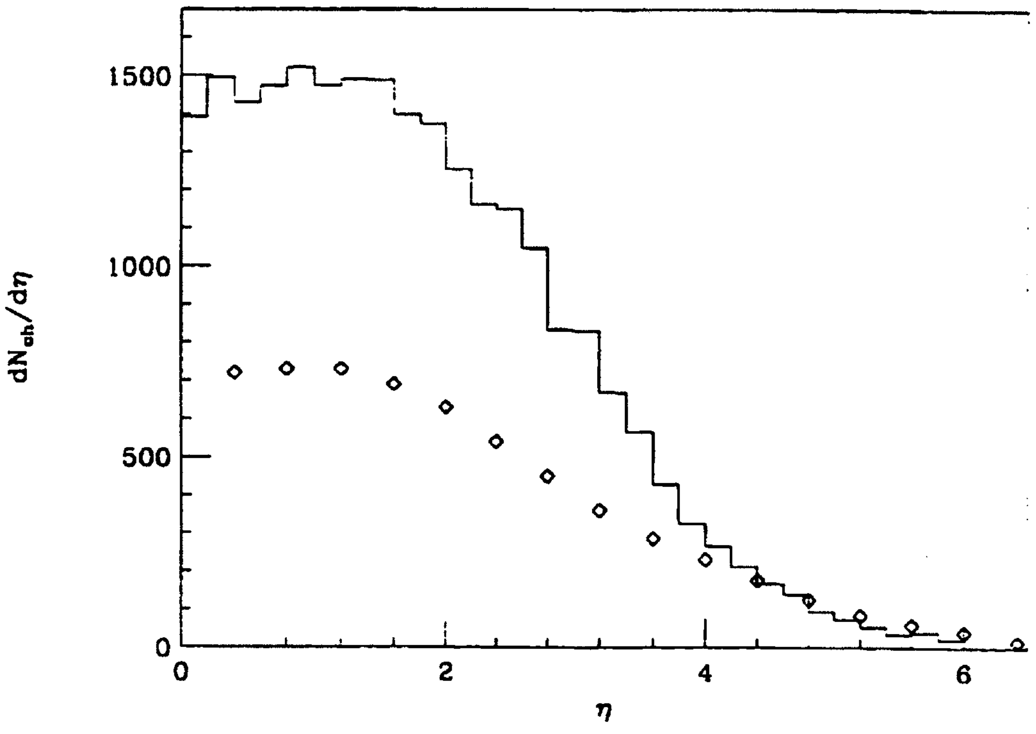

Figure 6.5: Charged particle pseudorapidity distribution for Au+Au with shadowing and secondary scattering (solid histogram) compared with HIJING [4] predictions (data points).

# Chapter 7

# Conclusions and Outlook

Within this thesis, several computer simulations were outlined and several studies were presented using computer simulations of relativistic heavy-ion collisions from CERN SPS energies to RHIC energies. At RHIC energies, a phase transition from hadronic matter to partonic matter is expected whereas at CERN SPS energies it is believed that the collisions are not able to create a dense enough medium for the phase transition to occur. Parton cascades as well as "background" simulations without deconfined partons were the models discussed. The latter simulation is used to study the low-mass lepton pairs excess discovered by the CERES [38] collaboration at CERN and simple hadronic observables at RHIC.

The utility of the simulation described does not end with the studies made within this thesis. The fact that this model gives full phase space information about the final state implies that it will be able to study many of the phenomena that will be measured at RHIC and LHC. Many studies and estimates have been made of dilepton observables at RHIC and LHC energies [77, 78, 79]. Examples of proposed phenomena that might give information on the nature of the phase transition between confined and deconfined matter include strangeness enhancement and $J/\Psi$ suppression [78, 79]. The total yield of $J/\Psi$ particles is proposed to be suppressed during a collision where a QGP is formed. When a QGP is formed, the quarks are free to interact with one another as long as the energy density is high enough. The $c$ and $\bar{c}$ quarks produced mainly through $gg$ scattering will most likely scatter with other quarks/gluons before they can be recombined into a $c\bar{c}$ bound state (J/$\Psi$). The suppression of J/$\Psi$'s due to the presence of a QGP phase during the collision can only be detected if there is not a similar suppression present in the "background". Suppression of J/$\Psi$ particles, via rescattering effects, relative to Drell-Yan production and dilepton production from mini-jets can be fully investigated by this simulation. The theoretical as well as the computational simplicity of the model makes it an ideal tool for further investigations into high-energy heavy-ion collisions.

# Bibliography

[1] M. Gyulassy. *Quark Gluon Plasma-Advanced Series on Directions in High Energy Physics.* edited by R.C. Hwa. World Scientific 1990.

[2] K. Geiger. Comp. Phys. Commun. **104**. 70 (1997); K. Geiger and B Müller. Nucl. Phys. **A544**. 467c (1992); K. Geiger and B. Müller. Nucl. Phys. **B369**. 600 (1992).

[3] D.H. Boal. Phys. Rev. **C33**. 2206 (1986).

[4] X.-N. Wang. M. Gyulassy. Phys. Rev. D **44**. 3501 (1991).

[5] T. Sjöstrand. Comp. Phys. Commun. **82**. 74 (1994).

[6] R.P. Feynman. Phys. Rev. Lett. **23**. 1415 (1969); J.D. Bjorken and E.A. Paschos. Phys. Rev. **185**. 1975 (1969).

[7] E.D Bloom *et al.*. Phys. Rev. Lett. **23**. 930 (1969); M. Breidenbach et al. Phys. Rev. Lett. **23**. 935 (1969).

[8] O.W. Greenburg. Am. Journ. Physics **50**. 1074 (1982).

[9] M. Gell-Mann and Y. Ne'eman. *The Eight-Fold Way.* Benjamin. 1964.

[10] J.D. Bjorken. Phys. Rev. **179**. 1547 (1969); J.I. Friedman and H.W. Kendall. Ann. Rev. Nucl. Part. Sci. **22**. 203 (1972).

[11] D. Soper. hep-ph/9702203.

[12] H.D. Politzer. Phys. Rev. Lett. **30**, 1346 (1973); D. J. Gross and F. Wilczek, Phys. Rev. Lett **30**, 1343 (1973).

[13] G. Sterman. hep-ph/9606312.

[14] R. Brock *et al.*. Rev. Mod. Phys. 67, 157 (1995); CTEQ collaboration. *Handbook of Perturbative QCD*. 1993.

[15] V.N. Gribov and L.N. Lipatov. Sov. J. Nucl. Phys. 15. 78 (1971); G. Altarelli and G. Parisi. Nucl. Phys. **B126**. 298 (1977); Yu. L. Dokschitzer. Sov. Phys. JETP **46**. 641 (1977).

[16] H.L. Lai. J. Botts. J. Huston. J.G. Morfin. J.F. Owens. J. Qiu. W.K. Tung and H.Weerts. Phys. Rev. D **51**. 4763 (1995).

[17] H.L. Lai. J. Huston. S. Kuhlman. F. Olness. J. Owens. D. Soper. W.K. Tung and H.Weerts. Phys. Rev. D **55**. 1280 (1997).

[18] Version 2 CTEQ distribution function in a parameterized form. J. Botts. H.L. Lai. J.G. Morfin. J.F. Owens. J. Qiu. W.K. Tung and H.Weerts. CTEQ Collaboration.

[19] A. Donnachie and P.V. Landshoff. Phys. Lett. **B296** 227. (1992).

[20] T. Sjöstrand. Phys. Lett. **157B**. 321 (1985).

[21] H.U. Bengtsson and T. Sjöstrand. Comp. Phys. Commun. **46**. 43 (1987).

[22] B. Andersson. G. Gustafson. G. Ingleman. and T. Sjöstrand. Phys. Rep. bf 97. 31 (1983).

[23] H.U. Bengtsson. Comp. Phys. Commun. bf 31. 323 (1984).

[24] A. Makhlin. Wayne State preprint (1994).

[25] L. McLerran. *Quark Matter and Heavy-Ion Collisions: Bielefeld Workshop 1982* World Scientific. 63.

[26] G. Kortemeyer. J. Murray. S. Pratt. K. Haglin. and W. Bauer. Phys. Rev. **C52**. 2714 (1995).

[27] J.P. Blaizot. R. Venugopalan. and M. Prakash. Phys. Rev. **D45**. 814 (1992).

[28] G. Sterman. *An Introduction to Quantum Field Theory*. Cambridge University Press. 48 (1993).

[29] P. Carruthers. Phys. Rev. Lett. **50**. 1179 (1983).

[30] L. Xiong and E.V. Shuryak. Phys. Rev. **C49**. 2203 (1994).

[31] L. McLerran and R. Venugopalan. Phys Rev. **D49**. 3352 (1994): **D50**. 2225 (1994).

[32] P. Siemens. M. Soyeur. and G. White. Phys. Rev. **C40** . 2641(1989).

[33] A.D. Jackson and H. Boggild. Nucl. Phys. **A470**. 669 (1987).

[34] C. DeMarzo. *et al.*. Phys. Rev. **D26**. 1019 (1982).

[35] NA35 Collaboration. H. Ströbele. *et al.*. Z. Phys. **C38**. 89 (1988).

[36] R. Santo *et al.*, Nucl. Phys **A566**, 61c (1994).

[37] NA35 Collaboration. M. Gazdzicki. Nucl. Phys **590A**. 197c (1995); NA35 Collaboration. D. Röhrlich. Nucl. Phys. **A566**. 35c (1994).

[38] G. Agakichiev *et al.*. Phys. Rev. Lett. **75**. 1272 (1995): J.P. Wurn for the CERES Collaboration. Nucl. Phys. A **590**. 103c (1995): I. Tserruya. nucl. Phys. **A590**. 127c (1995); A. Drees. Nucl. Phys. **A610**. 536c (1996).

[39] W. Cassing. W. Ehehalt, and C.M. Ko, Phys. Lett. **B363**. 35 (1995).

[40] G.Q. Li. C. M. Ko, and G.E. Brown. Phys. Rev. Lett. **75**. 4007 (1995); Nucl. Phys. **A606**. 568 (1996); G.Q. Li, C.M. Ko. G.E. Brown. and H. Sorge. *ibid.* **A611**, 539 (1996); **A610**, 342 (1996); G.Q. Li. G.E. Brown. and C.M. Ko. nucl-th/9706022 (1997 LANL preprint).

[41] Srivasta. Sinha. and Gale. Phys. Rev. **C53**. R567 (1996).

[42] C. Koch and C. Song. Phys. Rev. **C54**. 1903 (1996): C. Song. V. Koch. S. H. Lee. and C. M. Ko. Phys. Lett. **B366**. 379 (1996).

[43] Z. Huang and X.-N. Wang, Phys. Lett. **B383**. 457 (1996).

[44] J. Steele. H. Yamagishi. I. Zahed. Phys. Lett. **B384**. 255 (1996).

[45] R. Rapp. G Chanfray. and J. Wambach. Phys. Rev. Lett. **76**. 368 (1996).

[46] J. Kapusta. D. Kharzeev. and L. McLerran. Phys. Rev. D **53**. 5034 (1996).

[47] R. Baier. M. Dirks. K. Redlich. Phys. Rev. **D55**. 4344 (1997).

[48] J. Sollfrank *et al.*, Phys. Rev. **C55**. 392 (1997).

[49] C. M. Hung and E. V. Shuryak. Phys. Rev. **C56**. 453 (1997).

[50] C. M. Ko. Q. Li, and R. Wang, Phys. Rev. Lett. **59**. 1084 (1987): C. M. Ko and Q. Li. Phys. Rev. **C37**, 2270 (1988).

[51] H. Sorge. H. Stöcker. and W. Greiner, Ann. Phys. 192. 266 (1989).

[52] A. Drees. Phys. Lett. **B388**. 380 (1996).

[53] A. Drees. Nucl. Phys. **A610**. 536c (1996).

[54] K. L. Haglin. Phys. Rev C **53** R2606 (1996).

[55] For first suggestions and preliminary results of the importance of this mechanisms. see. K. Haglin. proceedings of INT/RHIC Workshop *Electromagnetic Probes of Quark Gluon Plasma* 24–27. 1996: and proceedings of *International Workshop on Hadrons in Dense Matter*. GSI. Darmstadt. 3-5 July 1996.

[56] J.A. Dankowych et. al.. Phys. Rev. Lett. **38**. 580 (1981).

[57] J. Janssen. K. Holinde. and J. Speth . Phys. Rev. **C49**. 2763 (1994).

[58] L. Xiong. E. Shuryak and G.E. Brown. Phys. Rev. **D46**. 3798 (1992).

[59] K.L. Haglin and C. Gale. to be published.

[60] J. Kapusta. P. Lichard. and D. Seibert. Phys. Rev. **D44**. 2774 (1991).

[61] C. Gale. private communication.

[62] C. Song. Phys. Rev. **C47**. 2861 (1993).

[63] B. Holstein. Comm. Nucl. Part. Phys.. Vol. 19. 221. (1990).

[64] J.I. Kapusta. private communication.

[65] L. D. Landau and I. Ya. Pomeranchuk. Dokl. Akad. Nauk SSSR **92** 535.(1953); **92** 735 (1953).

[66] K. Haglin and S. Pratt. Phys. Lett. **B 328**. 255 (1994).

[67] W. Bauer. G.F. Bertsch. W. Cassing. and U. Mosel. Phys. Rev. C **34.** 2127 (1986).

[68] Particle Data Group. Phys. Rev. D **50**. Part I (1994).

[69] M. Masera for HELIOS/3 collaboration. Nucl. Phys. A 590. (1995).

[70] K. Haglin. C.M. Ko. proceedings of *International Conference on Soft Dilepton Production*. LBNL. August 1997.

[71] D.W. Duke. J.F. Owens. Phys Rev. **D26** (1982) 1600.

[72] European Muon Collaboration. J. Ashman *et al.*. Phys Lett. **B 202.** 603 (1988).

[73] S.J. Brodsky and H.J. Lu. Phys. Rev. Lett. 64. 1342 (1990).

[74] L.L. Frankfurt and M.I. Strikman. Phys Rep. 160. 235 (1988): Nucl. Phys. **B316**. 340 (1989): L.L. Frankfurt. M.I. Strikman. and S. Liuti. Phys Rev. Lett. 65. 1725 (1990).

[75] F.E. Close. J. Qiu. and R.G. Roberts. Phys. Rev. **D40**. 2820 (1989).

[76] A. H. Mueller and J. Qiu. Nucl. Phys **B268**. 427 (1986).

[77] D. Fein. Z. Huang, P. Valerio. I. Sarcevic. Phys. Rev. **C56**. 1637 (1997).

[78] H. Sorge. E. Shurayak. and I. Zahed hep-ph/9705324 (1997 LANL preprint).

[79] R. Vogt hep-ph/9708294 (1997 LANL preprint).

[80] F. Halzen. *Quarks and Leptons: An Introductory Course in Modern Particle Physics*, John Wiley & Sons. 1984.

[81] D. Griffiths. *Introduction to Elementary Particles* . John Wiley & Sons. 1987.

[82] T. Csörgő. J. Zimányi. J. Bondorf. H. Heiselberg. and S. Pratt. Phys. Lett. **B241**. 301 (1990).

[83] K. Geiger and B. Müller. Nucl. Phys. **B369**. 600 (1992).

[84] G.F. Bertsch and S. Das Gupta. Phys. Rep. **160, No. 4**. 189 (1988).

[85] R.D. Field. *Frontiers in Physics: Applications of Perturbative QCD*. Addison-Wesley. 1989.

[86] C.Y. Wong. *Introduction to High Energy Heavy-Ion Collisions*. World Scientific. 1994.

[87] Y.L. Dokshitzer. V.A. Khoze. A.H. Mueller. and S.I. Troyan. *Basics of Perturbative QCD*. Editions Frontières. 1991.

[88] G.E. Brown and M. Rho. Phys. Rev. Lett. 66. 2720 (1991).

[89] F.R. Brown. F.P. Butler. N.H. Christ. Z. Dong. W. Schaffer. L.I. Unger. and A. Vaccarino. Phys. Rev. Lett. **65**. 2491 (1990).

[90] J. Murray. G. Kortemeyer. S. Pratt. K. Haglin and W. Bauer. NSCL/Cyclotron Laboratory Annual Report. 61 (1993).

[91] G. Kortemeyer. J. Murray. S. Pratt. K. Haglin and W. Bauer. NSCL/Cyclotron Laboratory Annual Report. 63. 65 (1993).

[92] K. Geiger. Phys. Rev. **C49**. 3234 (1994).

[93] J.D. Bjorken, Phys. Rev. **D27**. 140 (1983).

[94] K. Geiger. Phys. Rev. Lett. **71**. No. 19. 3075 (1993).

[95] K. Geiger. Phys. Rev. **D47**. 133 (1993).

[96] G. Kortemeyer. J. Murray. S. Pratt. K. Haglin. and W. Bauer. NSCL Annual Report. 63 (1994).

[97] K.J. Eskola. Z. Phys. C **51**. 633 (1991).

[98] X.-N. Wang and M. Gyulassy. Phys. Rev. Lett. 68. 1480 (1992).

[99] K.J. Eskola. J. Qiu. and X.-N. Wang. Phys. Rev. Lett. 72. 36 (1994).